Automation in Construction 104 (2019) 360–382

Contents lists available at ScienceDirect

Automation in Construction

journal homepage: www.elsevier.com/locate/autcon

Non-destructive means and methods for structural diagnosis of masonry arch bridges

Luis Javier Sánchez-Aparicio[a,*], Álvaro Bautista-De Castro[a], Borja Conde[b], Pedro Carrasco[a], Luís F. Ramos[c]

[a] Department of Cartographic and Land Engineering, University of Salamanca, High Polytechnic School of Ávila, Hornos Caleros, 50, 05003, Ávila, (Spain)
[b] University of Vigo, School of Industrial Engineering, Department of Engineering Materials, Applied Mechanics and Construction, Vigo, Spain
[c] ISISE, Department of Civil Engineering, University of Minho, Campus de Azurém, 4800-058 Guimarães, Portugal

ARTICLE INFO

Keywords:
Historical constructions
Masonry arch bridge
Non-destructive testing
Terrestrial laser scanner
Sonic testing
Multichannel analysis of surface waves
Ground penetrating radar
Ambient vibration tests
Finite element method
Non-linear analysis

ABSTRACT

Within the precepts defended by the International Charter of Kraków, this paper aims at presenting a fully non-destructive multidisciplinary approach able to characterize masonry bridges at three different levels: i) geometrical level; ii) material level and; iii) structural level. To this end, this approach integrates the terrestrial laser scanner, the sonic and impact-echo methods, the ground penetrating radar and the multichannel analysis of surface waves. All these data are combined with reverse engineering procedures, allowing the creation of suitable as-built CAD models for advanced numerical simulations. Then, these numerical models are contrasted and updated through the data provided by the ambient vibration tests. To validate the methodology proposed in this paper, the Roman bridge of Avila was used as study case. This bridge shows a complex mixture of constructive techniques (masonry, cohesive material, *Opus Caementicium* and reinforced concrete). Thus, the numerical model was considered for performing predictive structural analysis.

1. Introduction

Among the wide variety of constructive typologies that make up our historical legacy, masonry arch bridges have been placed as one of the most important elements through history, being still an essential part within the current communication networks. Many of these ancient constructions are at present day enduring potentially destructive conditions due to new traffic loads, large vibrations, foundation settlements, extreme natural events (e.g., earthquakes, river overflows or floods) and environmental agents (e.g., the presence of high levels of moisture or melting salts) [1]. The combination of these effects progressively induces the deterioration of the materials and the development of damage phenomena such as cracks or permanent deformations [2–4]. Because of this it is necessary to carry out a comprehensive structural diagnosis in order to know the current and the future structural condition of these types of infrastructures and consequently, designing proper conservation or restoration actions.

Among the different numerical modeling strategies proposed so far to evaluate masonry arch bridges mechanical behavior, from the Limit Analysis theory to the Discrete Element Method, the Finite Element Method [4] has been considered as one of the most powerful. This approach has allowed to simulate successfully masonry bridges under different casuistic such as settlements [2], pier scours [5], seismic actions and live loads [6–10], being possible to replicate the damages that appears along the history of the construction [2,11].

Despite this potential, one of the major drawbacks of this computational modeling approach is that it requires extensive knowledge of the physical and mechanical properties of the materials present on the structure, and thus the need of using multidisciplinary approaches to collect the required input data [12]. Under this framework, several studies in the past have focused on the development of multidisciplinary strategies targeted to characterize masonry arch bridges at different levels [8,13–15]: i) at a geometrical level; ii) at a material level and; iii) at the structural system level.

Concerning the first level, i.e., the geometry, this type of construction is typically characterized by its high complexity in terms of size, location, and inner composition. To face these challenges, the most widespread sensors are the terrestrial laser scanner and digital cameras. Through the terrestrial laser scanning and the photogrammetric method, they are extensively used to determine the external envelope of this typology of bridges [13,15–21]. The product obtained from these geomatic sensors, the so-called point cloud, is then employed for the

* Corresponding author.
E-mail addresses: luisj@usal.es (L.J. Sánchez-Aparicio), alvarobautistadecastro@usal.es (Á. Bautista-De Castro), bconde@uvigo.es (B. Conde), retep81@usal.es (P. Carrasco), lramos@civil.uminho.pt (L.F. Ramos).

https://doi.org/10.1016/j.autcon.2019.04.021
Received 3 January 2019; Received in revised form 23 April 2019; Accepted 24 April 2019
0926-5805/ © 2019 Elsevier B.V. All rights reserved.

creation of CAD models suitable for structural analysis by means of the following approaches [22]: i) creation of CAD models based on sections and individual measurements coming from the point cloud obtained [8,11,17,21]; ii) meshing of the point cloud and creation of the CAD model based on the mesh [22–24] and; iii) creation of non-uniform rational b-splines from the point cloud [24,25]. Additionally, it is possible to find in the recent literature procedures able to exploit the concept of the point cloud voxelization such as the Cloud2FEM procedure proposed by Castellazzi et al. [11,26,27]. These procedures are able to generate a numerical mesh from the point cloud in a semi-automatic way. However, these methods require a point cloud with few holes and tend to generate numerical meshes with a large number of elements. Besides, the presence existing permanent deformations can hardly be captured by means of these methods. In contrast to these strategies, it is possible to find approaches based on the latest advances in reverse engineering. These approaches exploit methods such as the extrusion of surfaces or b-splines to represent CAD models in which it is possible to control the level of detail [12,28]. Complementary to these techniques, the ground penetrating radar method has also been extensively used in order to characterize the inner composition of masonry arch bridges, such as the thickness of the barrel vaults or the layering of the infill materials [6,13,19,20,29].

Regarding the second level, the characterization of the constituent materials, masonry arch bridges present two main components: i) the masonry and; ii) the infill. Firstly, the masonry is used to build the main load-bearing parts of the bridge, such as the barrel vaults, spandrel walls and piers as well as other secondary elements such as buttresses or cutwaters. Masonry mechanical properties can be characterized resorting to laboratory tests (e.g., compression tests) or even in-situ tests using the flat-jack tests. On the one hand, the first approach is very time-consuming, since it requires the confection of several masonry samples. On other hand, the flat-jack tests are invasive, requiring the preparation of a slot through which a thin envelope-like bladder is inserted and pressurized with a fluid. Thus, as an alternative, the sonic testing approach has recently emerged as a suitable non-destructive testing technique aimed at determining the physical and mechanical properties of masonry [19,30]. Secondly, the infill material helps by dispersing the loads coming from the road surface down to the vaults as well as in its stabilization by providing additional lateral stiffness. The contribution of the infill material to the overall bridge strength is generally high, being an important aspect that should be taken into account in the structural assessment procedure, as it has been highlighted in previous research works [8,10]. However, the accurate characterization of the physical and mechanical parameters of infill materials poses a great challenge nowadays, requiring the use of invasive techniques to extract samples [31], or even the use of other invasive methods such as the Ménard Pressuremeter tests to locally characterize the infill properties [6,32].

Finally, with regards to the third level, i.e., the characterization of the structural system at a global level, several authors have considered the ambient vibration tests as the most suitable technique for evaluating the global response of this type of structures [10,19,32]. This approach allows obtaining the dynamic response of the structure, namely its natural frequencies and mode shapes, under operational conditions. These dynamic properties can be posteriorly considered within a constrained optimization framework. This framework's main goal is obtaining a set of input values for the Finite Element model of the structure (e.g., Young's Modulus of the masonry or infill) so that model outcomes best fit the experimentally obtained response of the structure; thus better representing its current mechanical behavior in operational conditions [8,19,32].

According to the above mentioned, the success of any numerical simulation, and hence the ability to emit an accurate structural diagnosis, strongly depends on the knowledge of the different constructive elements and the physical and mechanical properties of the materials with which they are built. Under this basis, and inside the framework of the modern restoration theory based on the precepts defended by the International Charter of Kraków [33], this paper proposes a multidisciplinary approach, fully based on non-destructive methods, aimed at generating high-fidelity numerical models. To this end, the approach combines well-known methods in the structural evaluation of masonry bridges such as the terrestrial laser scanner or the ground penetrating radar [20,21,34] with other procedures able to overcome part of the main limitations of the current multidisciplinary approaches. Among these limitations, stand out: i) the capacity of characterizing, in-situ and from a non-destructive point of view, part of the mechanical properties of the masonry and the infill; ii) the use of additional tests able to supplement the information provided by the ground penetrating radar and; iii) a method, based on the latest advances in reverse engineering, able to generate as-built CAD models, that reproduces the current deformed state of the bridge.

To validate the proposed methodology, described and highlighted in the above text, the roman bridge of Avila (Castile and León, Spain) is used as a case study. This bridge was initially erected during the age of Trajan to connect the *Decumanus Maximus* of the city with its riverside. However, the presence of anthropic and environmental agents has promoted on the bridge intense changes, currently showing a mixture of constructive systems (roman, mediaeval and modern) and materials (stone and concrete solutions). Bearing this in mind, the paper is structured as follows: after this initial introduction, Section 2 briefly describes the masonry arch bridge chosen to validate the multidisciplinary approach. Section 3 exposes the experimental campaign carried out and the obtained results. Section 4 presents the method proposed to generate an accurate numerical simulation of the bridge. Section 5 evaluates the accuracy of the developed model by comparing simulation outcomes with the experimentally obtained dynamic behavior of the bridge. Section 6 provides and discusses the results of the safety evaluation of the bridge, and finally, in Section 7 the conclusions are drawn.

2. The Roman bridge over the Adaja river

2.1. Historical background

The Roman bridge over the Adaja river is located on the road of Extremadura in the city of Avila, Spain, specifically in the western part of its Mediaeval Wall (Fig. 1). Its origin can be attributed to the Roman epoch, presumably during the Trajan period (98-117 A.C.) due to its similarity, in terms of constructive techniques and design, with other roman bridges erected in the same epoch, such as the Alcantara or the Bibey bridges [35]. The construction of this infrastructure was motivated by the necessity of communicating the *Decumanus Maximus* of the roman city *Abula* with its riverside.

In the Mediaeval age, probably during the Muslim invasion of the Iberian Peninsula in the year 711 A.C., the upper part of the bridge was demolished with the purpose of isolating the city. From this demolition, the piers, the cutwaters and the beginning of some of the vaults have remained intact [35]. During the XIth century, the spandrel walls and the missing parts of the vaults were restored with ochre granite coming from the nearby quarry of "La Colilla". This type of granite was the most used in Avila during the Mediaeval age. However, due to the premature erosion that this kind of material suffers, periodic restoration works were carried out on the bridge, being highlighted the restoration actions carried out in the XIIIth century, in which the parapets were replaced with grey granite masonry (Fig. 1).

Between 1788 and 1900 several industrial buildings were annexed to the east part of the bridge (Fig. 2). These constructions were demolished around 1996 due to their deficient state of conservation, especially after the fire that took place in 1984 [36] After the demolition of these buildings, the upstream right side of the bridge was covered with natural soil in order to restore the urban environment (Fig. 2b).

Fig. 1. General view of the bridge: a) upstream and; b) downstream.

More recently, on August 21st, 1995, a heavy rainfall damaged the bridge. The damage was amplified by the increase of the infill pressures due to its saturation, partially collapsing the upstream spandrel wall (Fig. 3a). This collapse along with the bridge's overall deficient state of conservation determined the necessity of undertaking major restoration works. These works were carried out during that year, repairing the right side, the left pier of the major vault as well as the central voussoirs of all the minor barrel vaults (Fig. 3b). Additionally, the bridge's deck was completely reconstructed, adding a weather-tightening concrete slab of 15 cm with non-structural steel bars and a granite cobblestone pavement (Fig. 3c and d).

2.2. Constructive description of the bridge

The bridge has a total length of approximately 60.00 m and a total width of 4.14 m, presenting five vaults along its trace. These vaults have a rise/span ratio near to 0.50 (Fig. 4) (Table 1). Viewing the bridge from the upstream side and from West to East (from the road of Extremadura to the Mediaeval Wall), the barrel vaults 1/2/3/5 show an average span of 6.18 m. In turn, the barrel vault 4 shows higher dimensions with a span of 9.20 m (Fig. 4d). The most relevant geometrical features are shown in Table 1.

Moreover, this bridge was built over a narrowing of the waterway produced by a rock formation of granite which was used as foundation for the piers of the bridge (Fig. 4). These piers have rectangular shape with an average height of 3.50 m and an average width of 4.66 m, thereby presenting an average pier slenderness (pier height-pier width ratio) of 1.33. All the piers at their bases have triangular cross-section starlings, or cutwaters, facing the upstream side (Fig. 4d). These cutwaters have an average height of 2.58 m and an average width of 2.11 m.

Apart from the geometrical features of the barrel vaults, piers and cutwaters, one of the most remarkable features of this historical bridge is the presence of two types of masonry (Fig. 4). On one hand, grey granite masonry from the Roman period, except for the parapets, that date from the Mediaeval period. This masonry is located in the lower part of the bridge as well as in all bridge's cutwaters and it is made up by regular masonry blocks. On the other hand, the upper part of the spandrel walls and the barrel vaults is made up by a regular ochre granite masonry with mortar joints (Fig. 4c and d).

Concerning the infill of the bridge, the archaeological samples taken in 1995 revealed the presence of two infill layers: i) a roman concrete with large aggregate size (*Opus Caementicium*) from the foundation until approximately 2/3 of the vault's rise and; ii) a compacted cohesive infill with inclusions of large aggregates from the 2/3 of the vault's rise until the deck. Over this layer rests a 0.15 m-thick concrete layer and a grey granite cobblestone pavement made up by stone blocks whose dimensions are 0.10 × 0.20 × 0.10 m. These stone blocks are with cement mortar (Fig. 3 c and d). Concerning the parapets, they have an average thickness of approximately 0.38 m and an average height of 1.36 m.

2.3. Damage indicators analysis

Before performing the in-situ non-destructive tests, a damage mapping was carried out with the aim of assessing the bridge's current state of conservation. This procedure resulted in the following visual indicators of alteration (Fig. 5) (Fig. 6): i) material losses; ii) deformations; iii) salt crusts; iv) biological colonization; v) moisture; and vi) graffiti.

It is worth mentioning the material losses observed on the barrel vaults (Fig. 6a) and the spandrel walls (Fig. 6b). These pathologies are mainly attributed to the high porosity and low frost resistance of the ochre granite [38], which in combination with the environment and the mechanical and chemical behavior of the cement mortar are causing

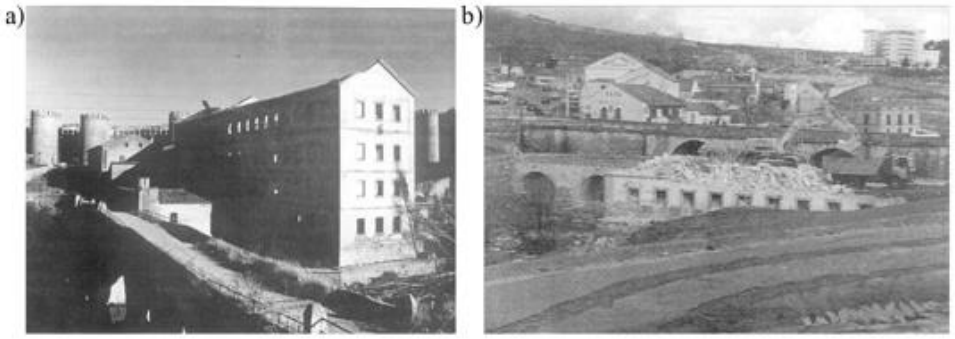

Fig. 2. Industrial buildings annexed to the upstream right side of the bridge [36]: a) view from the downstream and; b) image captured during the demolition of these buildings.

Fig. 3. State of conservation before the urgent restoration works carried out in 1995: a) general view of the east spandrel wall after the waterspout; b) state of conservation of the east barrel vault on which is possible to observe heavy material losses (in some sections around the 30% of the original thickness) and; c) and d) details of the granite cobblestone pavement added in 1995. Source: Memoria valorada para la actuación urgente en el Puente romano sobre el Río Adaja (Obras municipales 80/6).

material losses. This damage reduces the effective cross-section of the main load-bearing elements of the bridge. Also, it was possible to observe out-of-plane deformations in the upper part of the spandrel walls (Fig. 5).

3. Experimental program: geometrical, material and dynamical characterization of the bridge

Considering the necessity to determine all the structural components of the bridge, from both a geometrical and a mechanical point of view, the following multidisciplinary methodology was adopted (Fig. 7).

For the characterization of the external envelop of the bridge, it is proposed the use of the terrestrial laser scanner (TLS). Since this sensor is only able to capture the external geometry of the construction, the ground penetrating radar (GPR), the impact-echo method (IE) and the multichannel analysis of surface waves (MASW) are proposed as complementary sensors. In this case, the GPR and the IE method are employed to characterize the thicknesses of the spandrel walls and vaults. On the other hand, the MASW method is used to characterize the inner distribution of the infill. All information is later combined and used to create an as-built CAD model of the bridge by means of reverse engineering procedures.

From the material point of view, the proposed methodology uses the sonic testing for the characterization of the elastic properties of the masonry components. Meanwhile, the MASW method is used to characterize the Young Modulus as well as the density of the infill layers.

Finally, it is proposed the use of the Ambient Vibration Tests with the aim of validating the numerical simulation arose from the previous tests. Result of this combination of tests and procedures, it was possible to generate an accurate advance numerical simulation of the construction.

3.1. Geometrical characterization of the bridge

3.1.1. Terrestrial laser scanner survey

Due to the difficulty accessing some parts of the bridge, as well as to the complexity of its geometry, the use of the terrestrial laser scanning technology was the best solution, given its portability, accuracy and working range [12,39]. Accordingly, the Faro Focus 3D 120 equipment was used to characterize the geometrical envelope of the bridge (Fig. 8). This lightweight laser scanner is able to capture from 122,000 to 976,000 points per second with a nominal accuracy of 2 mm at 25 m.

Complementary to this sensor, several registration spheres, with two different diameters (200 mm and 145 mm), were used to perform an automatic alignment between the different scan stations. To this end, the target-based procedure defined by Franaszek et al. [40] was used.

As a result, a total of sixteen scans were required in order to record the whole bridge structure: i) ten scan stations to capture the downstream part of the bridge and; ii) six scan stations to represent its upper part, obtaining an alignment error of 0.005 ± 0.003 m. The huge amount of data captured was then reduced by applying a density filter with a threshold of 0.01 m. Therefore, an optimized 3D digitalization of the bridge made up by 15,631,250 points (representing the 32% of the total points captured during the experimental campaign) was finally obtained (Fig. 9).

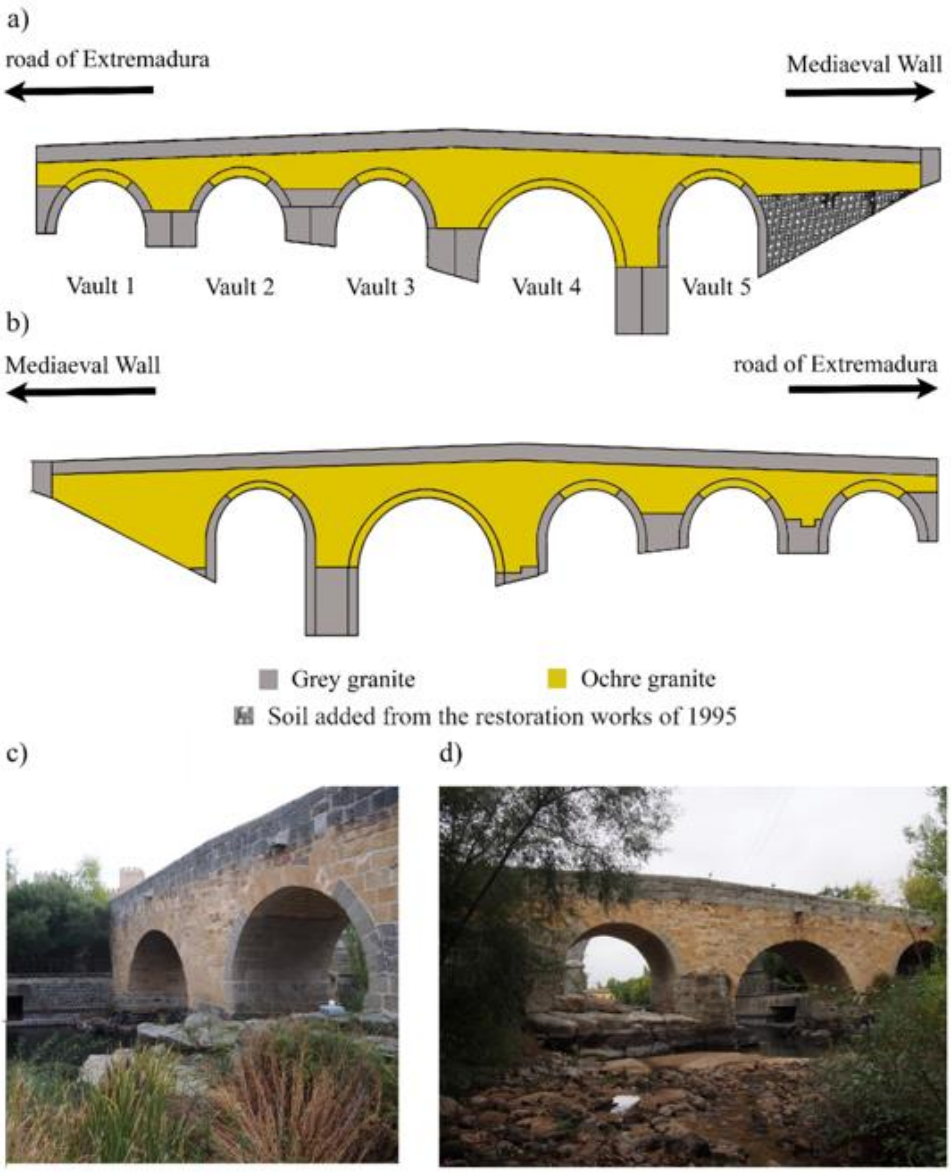

Fig. 4. Historical bridge over the Adaja river: a) downstream elevation; b) upstream elevation; c) general view of the upstream side and; d) general view of the downstream side.

Table 1
Geometrical features of the bridge barrel vaults.

Arch	Span (m)	Rise (m)	Rise/span ratio	Thickness (m)
1 (West)	6.17	3.04	0.49	0.55
2	6.19	3.03	0.49	0.54
3	6.19	3.03	0.49	0.53
4	9.20	4.86	0.53	0.85
5 (East)	6.15	3.05	0.50	0.55

3.1.2. Ground penetrating radar survey

Complementary to the TLS survey, the ground penetrating radar (GPR) method was used with the purpose to determine the inner structure of the bridge. To this end, the X3M® GPR system from MALA Geoscience was used, performing a total of five radargrams (Fig. 10): i) two horizontal profiles along the longitudinal axis of the bridge, with a central frequency of 250 MHz and a total time window of 30 ns and; ii) three profiles in the vertical direction with a central frequency of 800 MHz and a total time window of 100 ns. To scale the profiles, several marks were used during the data acquisition coinciding with the start and end points of each radargram.

On one hand, the vertical GPR profiles made it possible to determinethe cross-section of the bridge, which is made up by (Fig. 11): i) a 10.00 cm-thick granite cobblestone layer; ii) a 15.00 cm thick concrete slab; iii) a first infill layer from the concrete slab to 2/3 of the vault's rise (Mediaeval infill); iv) a second infill layer from 2/3 of the vault's rise until the foundation (Roman infill) and; v) a masonry foundation. These results were consistent with those obtained during the multichannel analysis of the surface waves test (Section 3.2.2) as well as with the archaeological samples (Section 2.2). Additionally, it

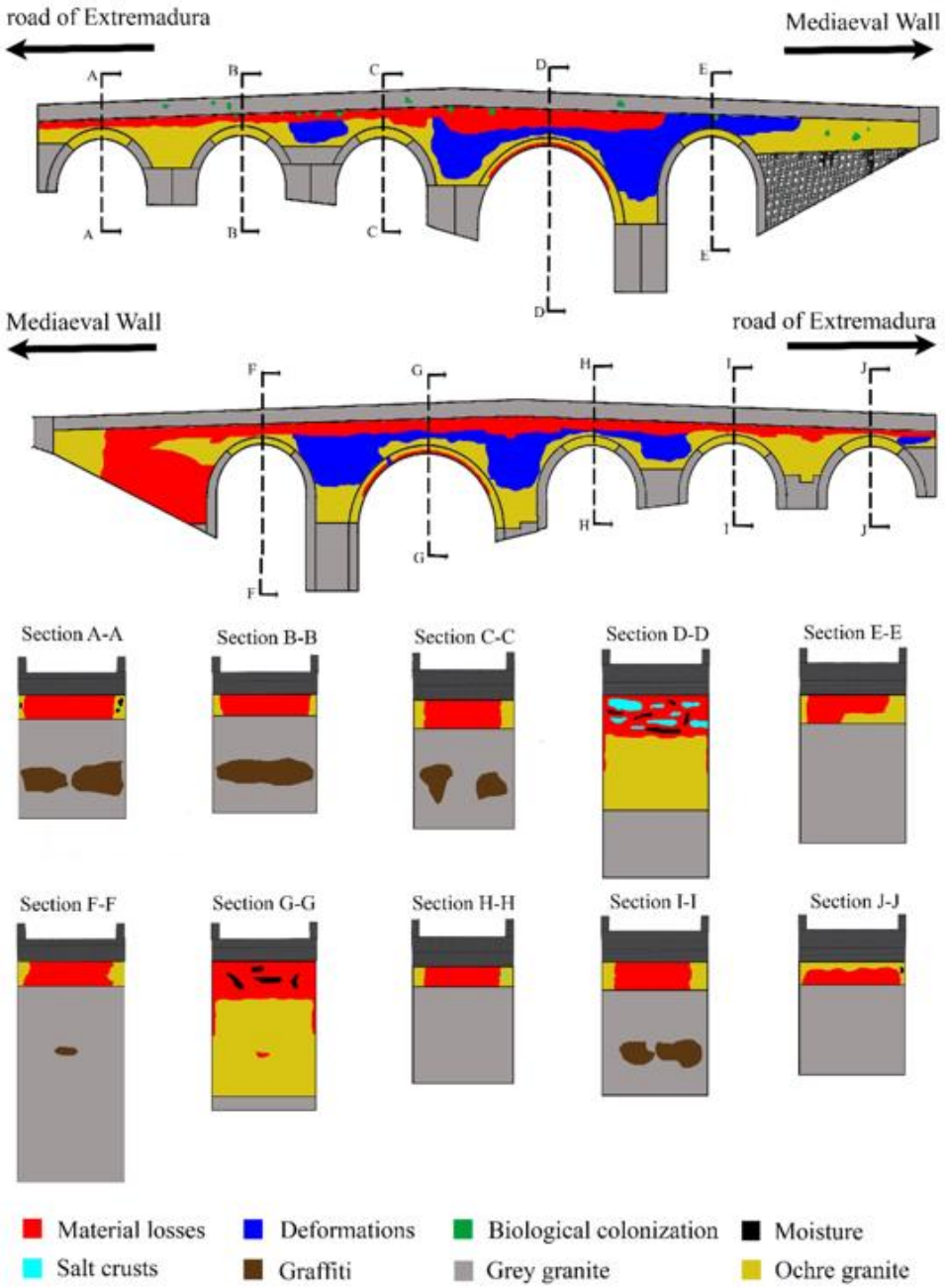

Fig. 5. Damage mapping obtained from the visual inspection performed according to the damage indicators defined within the framework of the European research project HeritageCARE [37].

was possible to estimate the thickness of the spandrel walls, with an average value of 0.45 m (Fig. 11).

On the other hand, the horizontal radargrams were characterized by the presence of a continuous reflection due to the presence of steel bars within the bridge's deck. These bars were used to avoid the presence of cracks due to the retraction of the concrete, having no influence from the structural point of view during the restoration works carried out in 1995. Thus, it was not possible to identify the infill distribution of the bridge (Fig. 12). Furthermore, it was possible to observe the presence of expansion joints equally spaced at 6.00 m along the concrete layer (Fig. 12).

3.1.3. Impact-echo tests

The impact-echo method was used to characterize the thickness of the masonry elements (spandrel walls and barrel vaults) and to verify the average thickness shown by the vertical profiles obtained from the GPR survey (Fig. 11). To perform these impact-echo tests, an equipment composed by the following elements was used: i) an instrumental hammer; ii) a data acquisition unit of 24 bit of resolution with a maximum sampling rate of 100 kHz and; iii) a transducer (piezoelectric

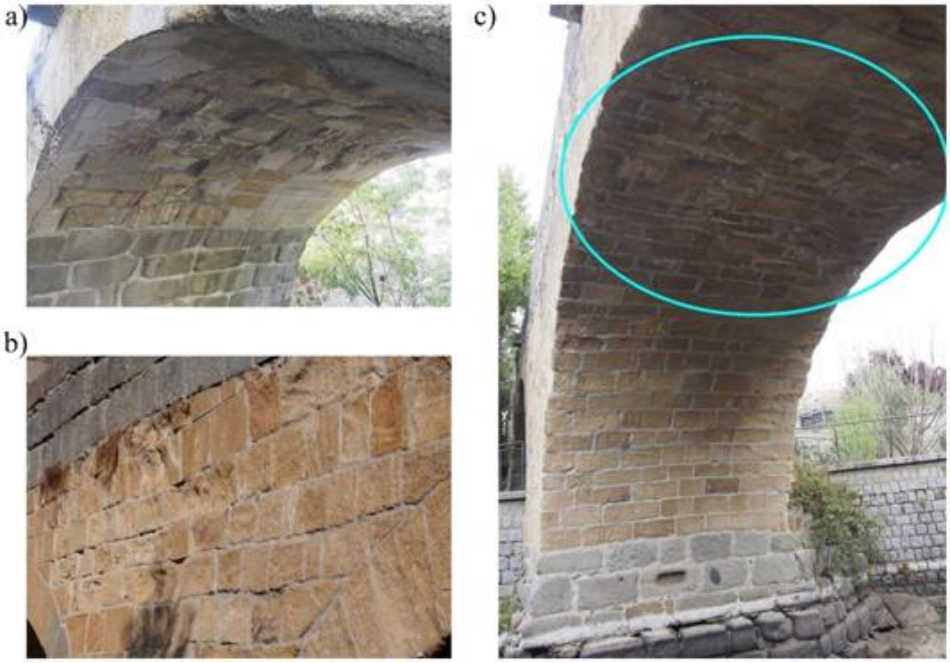

Fig. 6. Detail of the bridge's material losses caused by the aggressiveness of the environment and the cement mortar used to restore the masonry: a) keystone of the vault 5; b) upstream spandrel wall between the vaults 3 and 4 and; c) presence of white crusts on the main barrel vault keystone.

accelerometer) with a sensitivity of 10 V/g, range of ± 0.5 g and 8 μg of broadband resolution. It is worth mentioning that the instrumental hammer as well as the transducer was placed in the same position, making it possible to establish the starting and the ending point in the same location [41]. The excitation recorded by the transducer was then processed, and the frequency spectrum was then obtained through the use of the Fast Fourier Transform (FFT) [41]. The peaks detected by the FFT indicate the presence of internal heterogeneities which could be attributed to the interface between materials, in this case, masonry-infill.

Consequently, a total of six impact-echo tests were carried out on the bridge (Fig. 10b): i) three on the barrel vaults (stone 1 to stone 3) and; ii) three on the spandrel walls (stone 4 to stone 6). To extract the depth of the interface masonry-infill, the following equation was applied (Eq. 1).

$$V_p = 2df \tag{1}$$

where V_p is the P-wave velocity in m/s of the stone block and d is the distance in meters from the receptor to a point with a peak frequency f in Hz.

In order to obtain the propagation velocity of the P-waves (primary waves), several indirect sonic tests were carried out in the same position as the impact-echo tests. In this case, the hammer was placed at 0.50 m from the transducer (Fig. 10b). As expected, the propagation speeds obtained in the ochre granite were lower than the propagation speeds in the grey granite (11.82% lower) (see Table 2). This difference

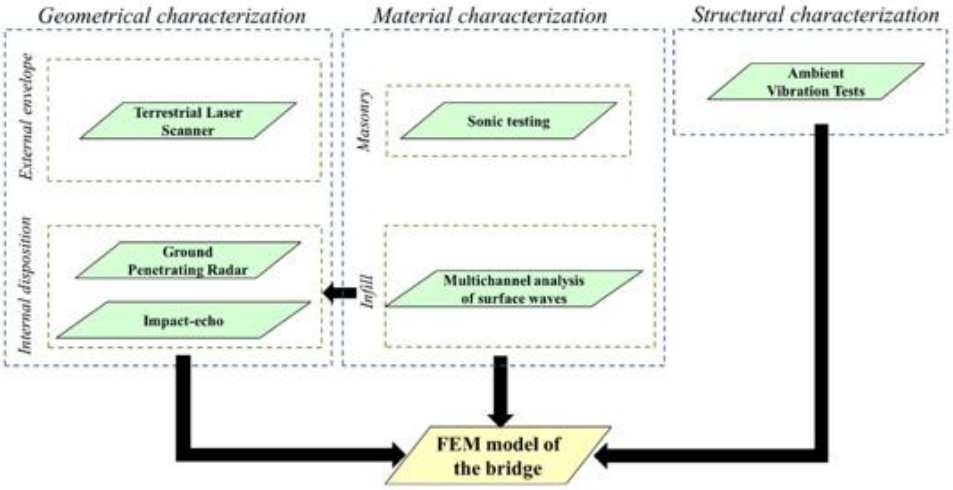

Fig. 7. The multidisciplinary methodology employed for the development of an advanced numerical simulation of the bridge.

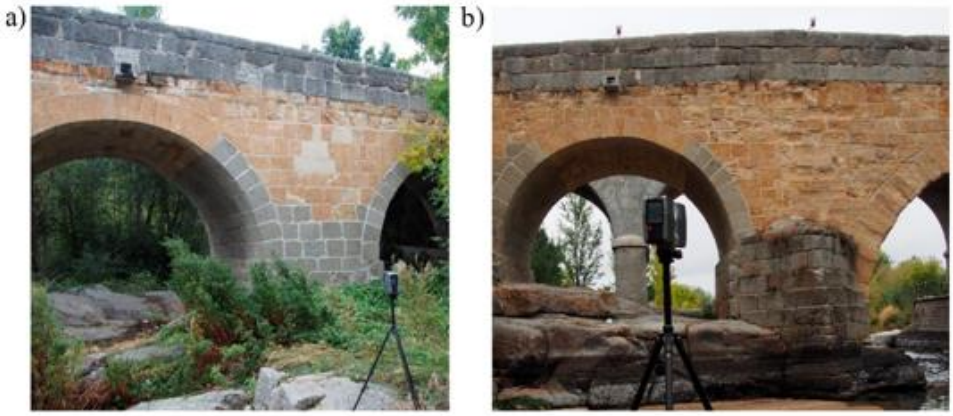

Fig. 8. TLS data acquisition: a) Faro Focus 3D and; b) detail of the registration spheres used to align the different scan stations.

can be attributed to the distinct nature of each kind of granite. While the grey specimen can be considered as an unaltered granite, the ochre granite is a silicified facie with more internal discontinuities [38].

The results of the impact-echo tests yielded an average thickness of 0.57 m in the barrel vaults and an average thickness of 0.47 m in the spandrel walls, being the thickness obtained in the spandrel walls consistent with the data provided by the vertical GPR profiles (Fig. 11) (Table 3).

3.2. Material characterization

3.2.1. Sonic testing

In order to obtain the mechanical properties of the two masonries identified during the visual inspection (Section 2.2), several indirect sonic tests were carried out in different areas of the bridge (Fig. 13). These tests were performed with the same equipment used in the indirect sonic testing carried out on the stone (Section 3.1.3).

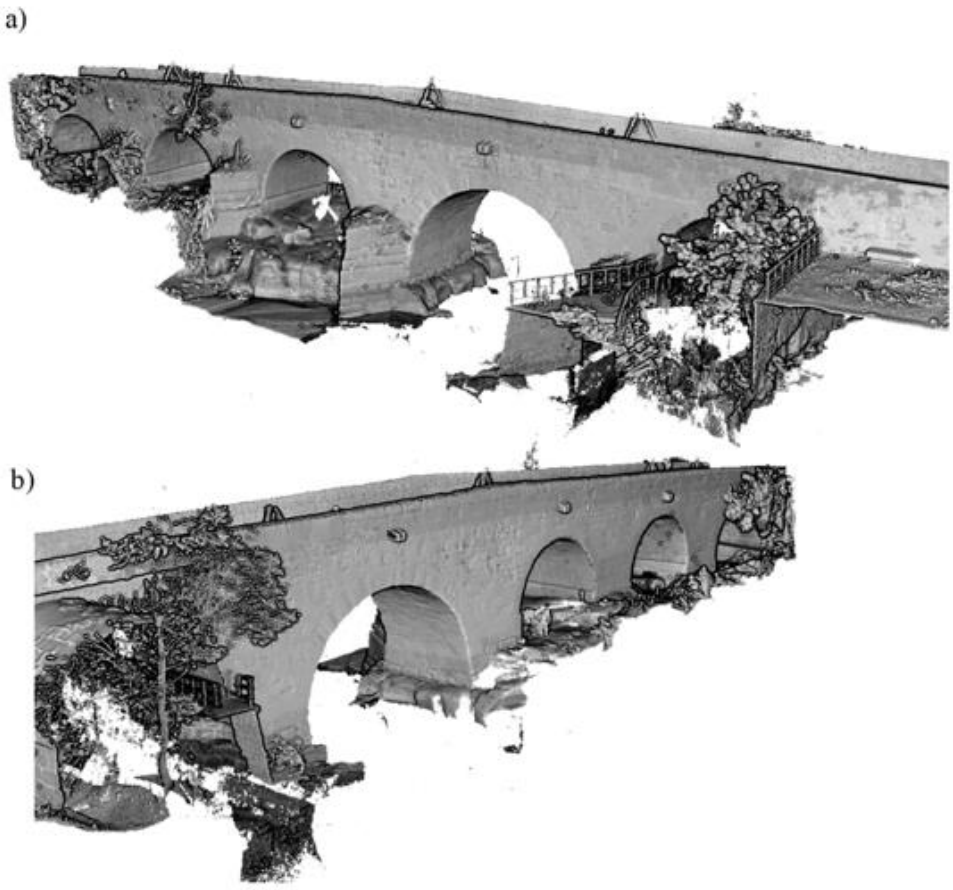

Fig. 9. General view of the bridge's point cloud obtained by the TLS: a) upstream side and; b) downstream side.

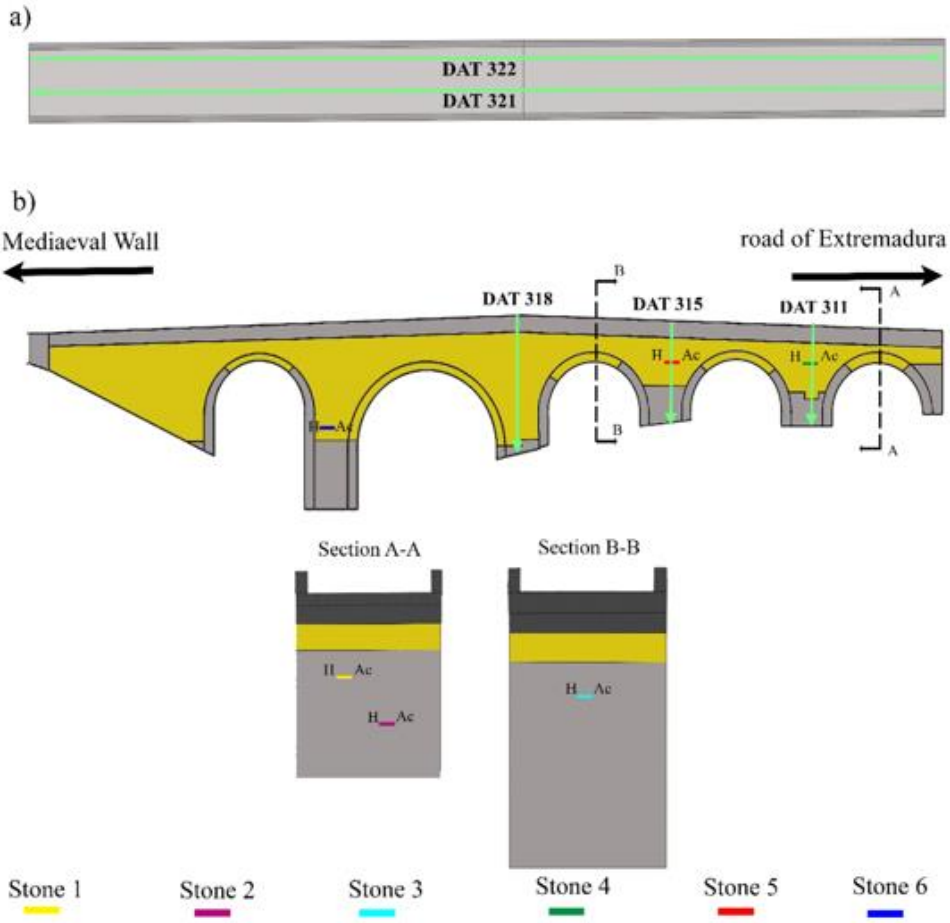

Fig. 10. Positions of the GPR, indirect and impact-echo tests carried out on the bridge: a) plant view and; b) downstream elevation. *H* indicates the position of the hammer and *Ac* indicates the position of the transducer during the indirect sonic tests.

On each evaluated area, the material was excited with the instrumental hammer, promoting the generation of compressional or primary waves (V_p) and surface or Rayleigh waves (V_r). The propagation velocity of these waves was obtained by measuring the time delay between the emission of the signal (impact of the instrumental hammer) and its reception by the transducer. Once the propagation velocity was estimated, it was possible to calculate the mechanical properties of the grey and ochre granite masonries using the following equations (Eqs. (2)–(4)) [42]:

$$V_P = \left(\frac{E(1-\nu)}{\rho(1-\nu)(1-2\nu)}\right)^{1/2} \quad (2)$$

$$V_r = \frac{0.87+1.12\nu}{1+\nu}\left(\frac{E}{2\rho(1+\nu)}\right)^{1/2} \quad (3)$$

$$\frac{V_p}{V_r} = \frac{0.87+1.12\nu}{1+\nu}\left(\frac{(1-2\nu)}{2(1-\nu)}\right)^{1/2} \quad (4)$$

where V_p is the velocity of propagation of the P-waves in m/s; V_r is the velocity of propagation of the R-waves in m/s; E is the Young's Modulus of the material in GPa; ρ is the density of the material in kg/m3 and; ν is the Poisson's coefficient of the material.

While the Poisson's ratio can be directly obtained from the relation between V_p and V_r (Eq. (4)), the masonry's Young's Modulus requires knowing the density (Eqs. (2)–(3)). The density of the grey granite masonry was assumed between 2000 kg/m^3 to 2500 kg/m^3 [19]. Meanwhile, the density of the ochre granite masonry was assumed between 1700 kg/m^3 to 2000 kg/m^3. This assumption was based on the experimental tests carried out by Garcia-Talegon et al. [38] on the ochre granite of Ávila.

Table 4 shows the results of the indirect sonic tests carried out on the masonries. On one hand, the grey masonry showed average propagation velocities values of 1316.56 m/s and 697.78 m/s for the P and R-waves, respectively, yielding a Young Modulus comprised between 2.90 and 3.60 GPa. On the other hand, lower propagation speeds from the ochre masonry were observed (1202.69 m/s for the P-waves and 601.51 m/s for the R-waves) and therefore, a lower Young Modulus, which ranged from 2.05 GPa to 2.41 GPa.

3.2.2. Multichannel analysis of surface waves

The infill material of a masonry arch bridge can be considered as soil inserted within the space delimited by the spandrel walls, vaults, and piers. Under this assumption, Geophysics can offer a wide variety of techniques able to characterize soils from a geometrical, physical and mechanical point of view [43]. Within this context, the multichannel analysis of surface waves (MASW) stands out. This approach allows obtaining a 2D profile, represented by the plane generated between the geophones, the instrumental hammer, and the *z* direction of the phase velocities and frequencies of the waves generated after the excitation of a soil (dispersion curve) [44]. The fundamental mode of the dispersion

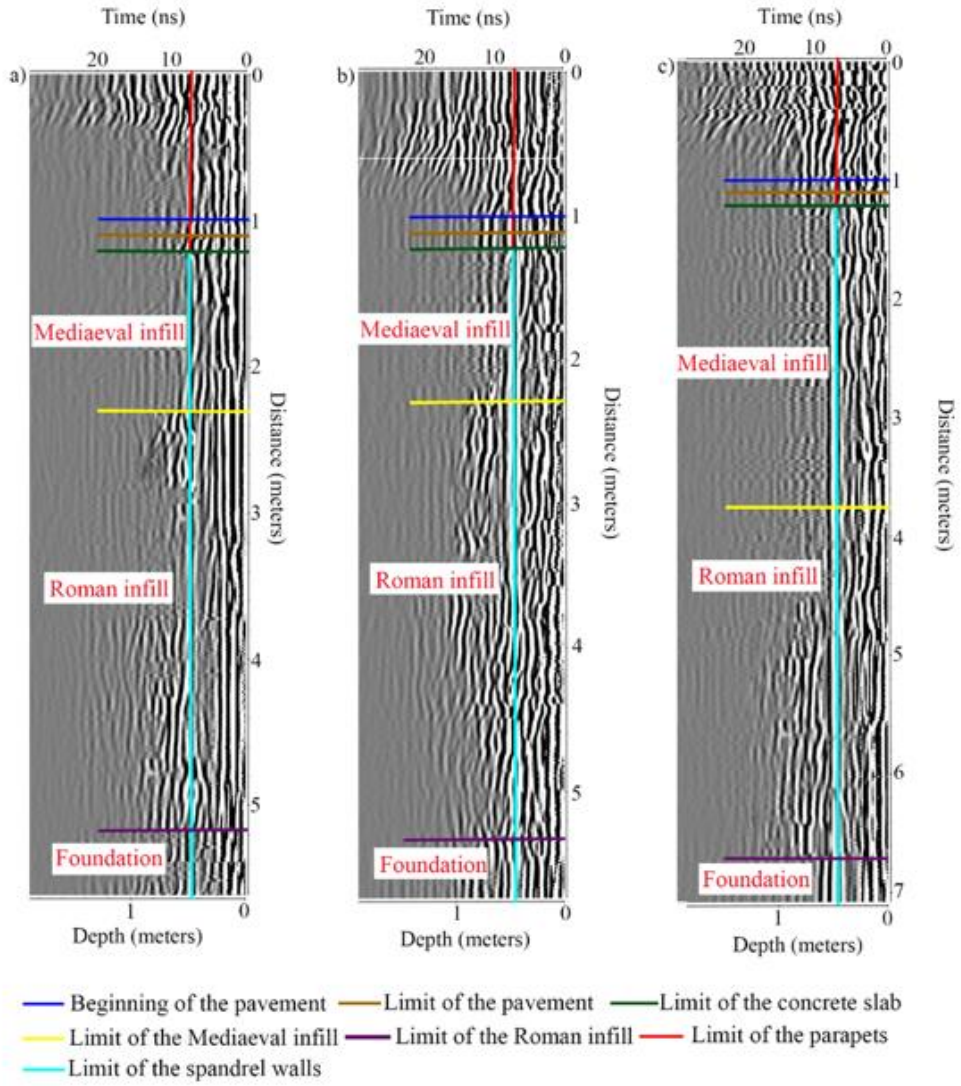

Fig. 11. Results obtained from the vertical GPR profiles: a) radargram DAT-31; b) radargram DAT-315 and; c) radargram DAT-318.

curve is extracted, and an optimization process, also called inversion analysis, is carried out with the aim of obtaining the shear-wave velocities of the soil (V_s) [45]. Additionally, it is possible to capture the primary-wave velocities (V_p) generated during the excitation of the soil [44]. Thus, the MASW method allows obtaining a 2D plot of the average shear and primary-wave velocities of a soil in relation to the position of the linear array of geophones and the z axis. Then, both velocities are linked with the Young Modulus and density of the soil as follows (Eqs. (5)–(6)):

$$\rho = 1.2475 + 0.399\left(V_p/1000\right) - 0.026\left(V_p/1000\right)^2 \quad (5)$$

$$E = \rho V_s^2 \frac{3\left(\frac{V_p}{V_s}\right)^2 - 4}{\left(\frac{V_p}{V_s}\right)^2 - 1} \quad (6)$$

where ρ is the density in kg/m^3; E is the Young's Modulus in GPa; V_p is the primary-wave velocity of the soil in m/s and; V_s is the shear-wave velocity of the soil in m/s.

Taking into account all the above mentioned, a MASW test was carried out on the east part of the bridge (Mediaeval Wall) (Fig. 14a). The excitation of the soil was carried out using a 20.00 kg sledge-hammer connected to a data acquisition unit (Fig. 14b, c). The excitation was captured by a linear array of 20 geophones equally spaced (0.40 between each one of them in a total length of 7.60 m) (Fig. 14a) and connected to the data acquisition unit.

Table 5 shows the results obtained from the MASW test. From the *Vs* values it was possible to obtain a first estimation of the bridge's infill layers (Fig. 15) (Table 5): i) one layer, with a depth of approximately 1.76 m, made up by a compacted material with an average Young's Modulus of 0.43 GPa and; ii) a second infill layer with an average Young's Modulus of 1.03 GPa, ranging from first infill layer's bottom to the foundation of the bridge. These values seem to be consistent with those obtained by the archaeological samples (Section 2.2) as well as with the values found in the existing literature [8,46,47].

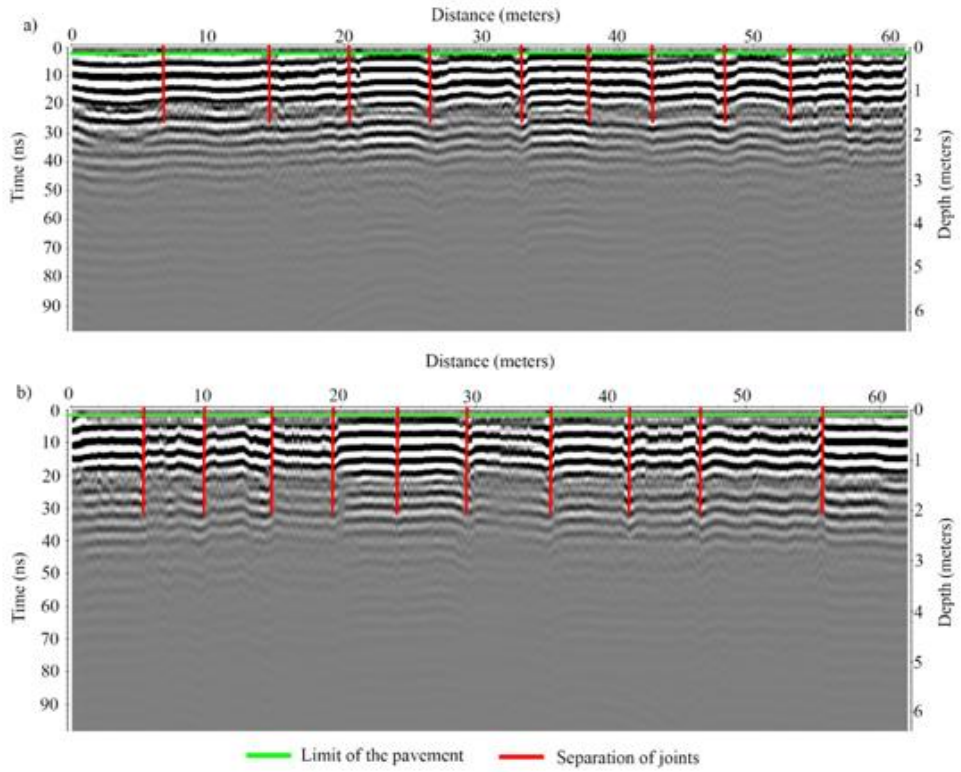

Fig. 12. Results obtained from the horizontal GPR profiles: a) radargram DAT-321 and; b) radargram DAT-322.

Table 2
Propagation velocities obtained during the experimental campaign in each type of granite.

Sample		Propagation speed			
		V_p (m/s)	Cov (%)	V_r (m/s)	Cov (%)
Grey granite	Stone 1	1282.60	1.61	679.78	1.57
	Stone 2	1297.80	1.53	687.73	1.20
	Stone 3	1286.40	1.38	681.79	1.60
Ochre granite	Stone 4	1137.44	1.33	602.84	1.29
	Stone 5	1138.46	1.97	603.38	1.40
	Stone 6	1133.55	1.02	600.78	1.59

Table 3
Results obtained from the impact-echo tests and comparison of the thicknesses data with their counterparts obtained from the vertical GPR profiles. In brackets the covariance, in %, of the frequencies obtained during the impact-echo tests.

Samples		V_p (m/s)	Thickness (m)	
			Impact-echo	GPR
Grey granite (barrel vaults)	Stone 1	1282.60	0.56	–
	Stone 2	1297.80	0.58	–
	Stone 3	1286.40	0.56	–
Ochre granite (spandrel walls)	Stone 4	1137.44	0.51	0.45
	Stone 5	1138.46	0.45	0.45
	Stone 6	1133.55	0.45	0.45

3.3. Dynamic identification

With the aim of identifying the dynamic properties of the bridge (natural frequencies and modal displacements), an ambient vibration test (AVT) was also performed in the last stage of the in-situ non-destructive survey. To achieve reliable results, several numerical simulations, adopting different boundary conditions, were previously performed. This way, it was possible to arrange the most proper configuration for the AVT test as well as the identification of the most appropriate areas to place the accelerometers (Fig. 16).

To determine the dynamic properties of the bridge, the Enhanced Frequency Domain Decomposition algorithm (EFDD), based on the power spectral density, was applied [48]. Consequently, a total of seven mode shapes were successfully identified along with their corresponding frequencies, ranging between 10.29 Hz to 31.90 Hz [8] (Table 6).

For this case study, it is worth mentioning the high frequencies obtained in comparison with similar tests carried out in other masonry bridges (Table 6). These values are suggestive of a structure with a high stiffness/mass ratio which can be explained by the presence of a reinforced concrete slab on the deck, a high-quality infill and the use of a light-weight masonry (ochre granite).

It is worth mentioning that the accelerometers used to capture the dynamic response of the bridge were placed mainly in the z and the y direction in order to capture the weak direction (out-of-plane) as well as the vertical response of the structure. This type of setup is similar to those adopted in other experimental campaigns [8,16].

4. Numerical model

4.1. Point cloud registration

Previous to the generation of the geometrical CAD model, the registration strategy defined by Bautista-De Castro et al. [12] was applied. This approach allows registering the longitudinal axis of the bridge's point cloud with the x-axis of the global coordinate system, and thus the

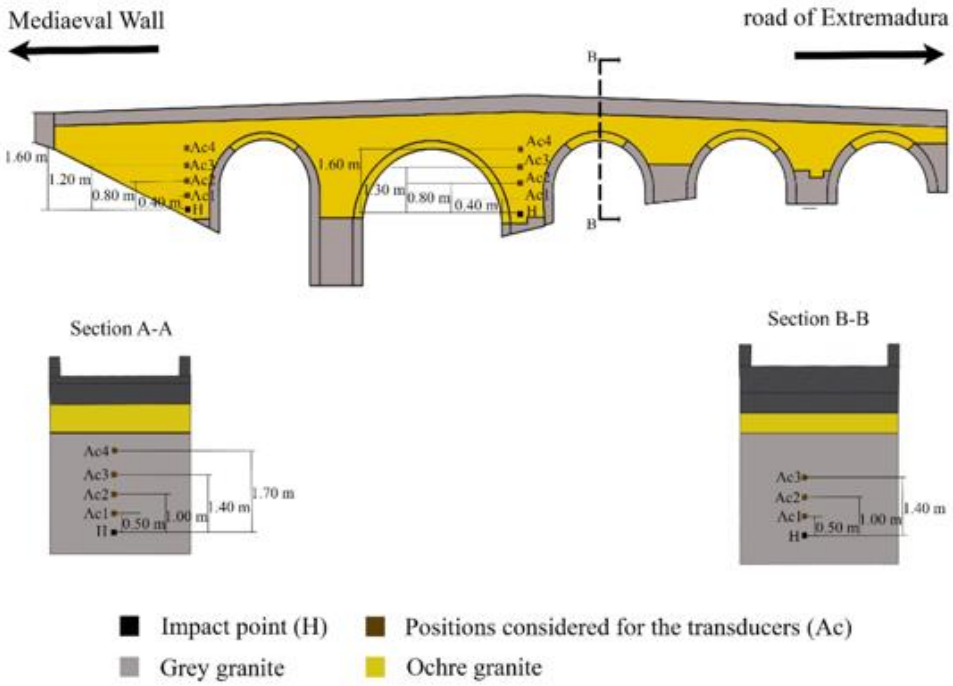

Fig. 13. Layout considered for the sonic testing.

Table 4
Results obtained from the indirect sonic tests.

	Ochre granite		Grey granite	
	P-wave	R-wave	P-wave	R-wave
Average velocity (m/s)	1202.69	601.51	1316.56	697.78
CoV (%)	1.42	1.79	1.48	1.57
Poisson's coefficient	0.26		0.24	
Density (kg/m^3)	1700–2000		2000–2500	
Young's modulus (GPa)	2.05–2.41		2.90–3.60	

correct integration of the different captured data (e.g. AVT). To this end, the following steps were carried out (Fig. 17): i) extraction of the covariance matrix (Eqs. (7)–(80); ii) Eigenvalue analysis of the covariance matrix (Eq. (9)); iii) evaluation of the angle between the Eigenvector associated with the maximum Eigenvalue and the *x*-axis of the global coordinate system and; iv) a *z* rotation of the global point cloud.

$$C = \frac{\sum_{p_i \in P} w_i (p_i - \overline{p})^T (p_i - \overline{p})}{\sum_{i=1}^{n} w_i} \tag{7}$$

$$\overline{p} = \sum_{i=1}^{n} P_i / n \tag{8}$$

$$V^{-1} C V = D \tag{9}$$

where C is the covariance matrix of the point cloud P; w_i is the weight associated to each point p_i; $\overline{p}$ represents the mean of the points; V is an orthogonal matrix that contains the corresponding eigenvectors and; D is the diagonal matrix containing the eigenvalues. For the present case study, the same unit weight was assumed for each point.

4.2. Creation of the as-built CAD model

According to Sánchez-Aparicio et al. [25], the creation of a suitable CAD model for numerical analysis purposes can be carried out by means of the following strategies: i) extraction of orthogonal views and sections over several directions of the point cloud or mesh or; ii) by means of advanced surface representation methods such as the non-uniform b-splines, allowing the representation of complex surfaces. Taking into consideration the out-of-plane deformations observed during the visual inspection (Section 2.3), the second approach was deemed as the most adequate, being carried out through the following workflow (Fig. 18): i) 3D Delaunay triangulation; ii) extraction of sections, spaced 1.00 m, along the *x*-axis; iii) vectorization of each section by means of b-spline curves and; iv) creation of a solid geometrical model based on Loft surfaces, considering the b-splines as its directrix curves [49].

As a result, it was possible to construct a rough solid model of the bridge envelope on which the out-of-plane deformations observed on the spandrel walls were accurately captured. To refine this model, including the barrel vaults and other bridge elements such as the infill layers, several Boolean operations were carried out at a later stage [49], intersecting parametric shapes (e.g., cylinders for the barrel vaults and planes for the definition of the boundaries and materials) with the envelope obtained in the previous stage (Fig. 18). It is worth mentioning that the interface between infills was modeled based on the data provided by the GPR and the MASW tests. Meanwhile, the thickness of the spandrel walls was modeled assuming a fixed average value, estimated in 0.46 m, obtained from the vertical GPR profiles as well as the impact-echo tests (Table 3).

The previously defined reverse engineering procedure allowed obtaining a highly detailed solid CAD model. However, and considering the focus of the present study, the creation of an accurate numerical model of the bridge, the cutwaters were omitted at this stage and later integrated during the generation of the finite element mesh.

4.3. Finite element mesh

With from the previously created geometrical model as a starting point, a finite element mesh was generated using the FEM software TNO Diana® [50] (Fig. 19). This mesh was comprised of 86,418 solid elements and 166,292 degrees of freedom, including two elements along

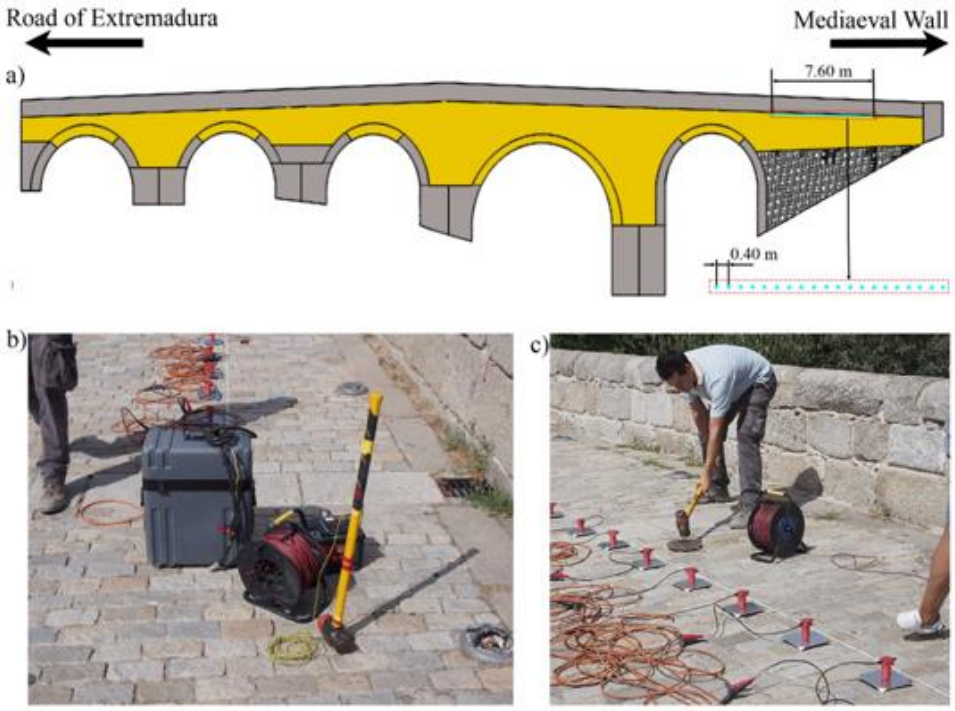

Fig. 14. MASW tests: a) setup; b) detail of the used equipment and; c) moment when the infill is excited. Array of geophones used during this test in blue. (For interpretation of the references to colour in this figure legend, the reader is referred to the web version of this article.)

Table 5
Values obtained for the two infill layers identified on the bridge. UB denotes the upper bound value and LB the lower bound value.

	First layer		Second layer	
	UB	LB	UB	LB
V_p (m/s)	1451.4	1427.3	1705.2	1606.7
V_s (m/s)	316.1	294.7	515.0	419.6
E (GPa)	0.52	0.45	0.84	1.28
ρ (kg/m3)	1771	1764	1852	1821

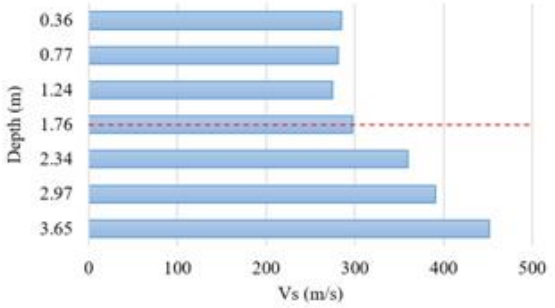

Fig. 15. Graphical representation of the relation between the depth and the V_s speeds. The red line represents the interface between the different bridge's infill layers. (For interpretation of the references to colour in this figure legend, the reader is referred to the web version of this article.)

the thickness of the spandrel walls and barrel vaults in order to correctly capture stress gradients in subsequent non-linear structural analysis. It is worth mentioning that the cutwaters were defined through extrusions, considering a geometry with an equivalent stiffness (Fig. 19). The concrete slab, as well as the granite cobblestone, was included in the model by means of extrusion of the bridge's deck. These extrusions were made without any connection with the spandrel walls as it was observed during the visual inspection.

Concerning the boundary conditions, they were applied in agreement with the surrounding medium of the bridge: pinned supports at the base, abutments, and the spandrel wall covered by the soil added in 1995 (Figs. 4, 5).

As for the material properties of the masonry and infill, they were defined according to the values obtained during the experimental campaign (Tables 7, 8). Meanwhile, the materials of the bridge's deck were defined according to the data provided by the last restoration project (Table 9): a granite cobblestone pavement joined with a cement mortar upon a concrete slab. On one hand, the homogenized Young's Modulus of the granite cobblestone was set according to the equations defined by the Eurocode 6 [51] and the experimental data obtained by Garcia-Talegón et al. [52]. On the other hand, the mechanical and physical properties of the concrete slab were defined according to the Eurocode 2 [53], considering a characteristic compressive strength of 16 N/mm^2 (C 16/20). It is worth mentioning that the steel bars detected by means of the horizontal radargrams were not included in the numerical simulation since they not have a structural function.

5. Evaluation of the discrepancies between the numerical model and the experimental modal data

One of the factors explaining the widespread employment of the FEM method in the analysis of masonry structures is the possibility of simulating complex scenarios such as earthquakes or settlements. However, the quality of the output results obtained from these simulations is strongly influenced by the uncertainties associated with the mechanical properties of the materials, the correct definition of the structure's boundary conditions, and the geometrical simplifications incurred when developing the numerical model. Therefore, these

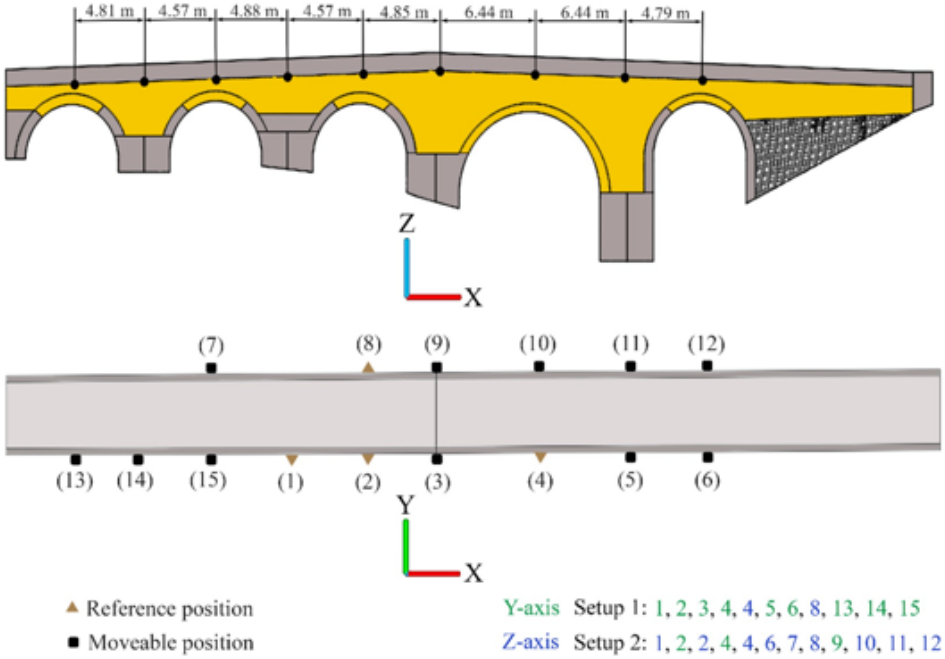

Fig. 16. Schematic representation of the setups carried out during the AVT test.

Table 6
Natural frequencies and mode shapes obtained from the AVT tests.

Mode	Natural frequency (Hz)	Description of the modal shape
1	10.30	Translational mode in the *x* axis
2	14.57	Torsional model in the *x* axis
3	21.09	Translational mode in the *z* axis
4	24.13	Torsional model in the *y* axis
5	26.31	Torsional and translational mode in the *x* and *z* axis respectively
6	29.45	Torsional model in the *x* axis
7	31.90	Torsional model in the *y* and *x* axis

aspects demand the use of suitable strategies able to validate these numerical simulations.

Taking all of this into account, a preliminary numerical simulation (Eigen-value analysis) was carried out with the average values of the different materials present on the structure (Tables 7, 8, 9). In order to evaluate the accuracy of the numerical simulation, the error between frequencies and the modal assurance criterion (MAC) [54] (Table 10) was considered as quality indicators.

The results obtained from this initial numerical simulation showed a more flexible structure in comparison with the real one (with an average error in frequencies of 5.03%), suggesting the need to perform a calibration or model updating procedure to improve the discrepancies (Table 10). As for the MAC values, it was possible to observe a fairly good match at the exception of the 7th mode.

Thereby, manual calibration of the numerical model was carried out by modifying the Young's Modulus of the infill layers and masonries within the possible range of values determined by the upper and lower bounds determined by the experimental campaign (Tables 7, 8). Moreover, to mimic the real response of the structure with greater fidelity, a possible interaction effect between the east part of the bridge and the infill soil added in 1996 was considered. For this particular case, a range of admissible stiffness comprised between 1×10^7 N/m^3 and 1×10^9 N/m^3 according to Bautista-De Castro et al. [12] was defined. As a result, it was possible to obtain a numerical simulation whose dynamic response closely matched the dynamic response captured by the AVT tests (Tables 11, 12) (Fig. 20). Thus, the updated numerical model showed an average error in frequencies of 2.22% and an average modal assurance criterion of 0.91 (Table 12).

It is worth mentioning the asymmetric dynamic response of the bridge in Mode I and II. This phenomenon can be attributed to the structural disposition of the bridge on which the major barrel vault, which is 1.5 times thicker and 3 times longer in terms of span (Table 1), is not in the center of the structure (Fig. 4).

The good quality of masonry as well as the well-shaped ashlars found in the spandrel walls, cutwaters, and vaults are consistent with the values obtained during the sonic tests and the calibration of the numerical model (Fig. 4b, c) (Table 12). As expected, the calibration procedure pointed out a non-negligible interaction effect between the soil added in 1995 and the east part of the bridge (Fig. 1b) (Table 12). Finally, regarding the infill layers, it was possible to corroborate again the presence of a high-quality infill material in most of the structure, which lays in the Roman parts of the bridge, and which is also consistent with the data provided by the archaeological samples taken during 1995.

6. Structural assessment

6.1. Modeling assumptions

In the developed computational model, the non-linear behavior of the masonries (grey and ochre granite) was modeled by adopting the total strain rotating crack model (TSRCM), implemented in the Finite Element software TNO Diana [50]. A post-peak exponential softening for tensile behavior and a parabolic hardening followed by a post-peak parabolic and exponential softening for compression were respectively adopted. To estimate the inelastic parameters describing the masonry nonlinear behavior, the following criteria was considered for both types of masonries: i) the compressive strength value was considered as 1000 times the corresponding Young's Modulus, as proposed by Tomazevic

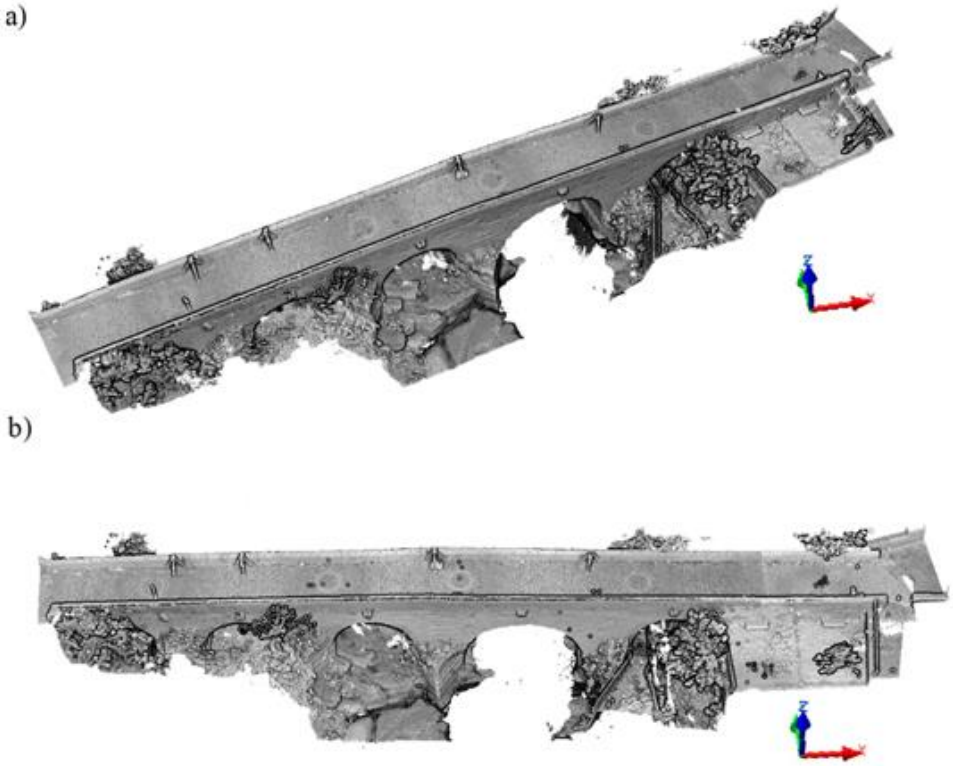

Fig. 17. Point cloud of the bridge: a) before registration and; b) after registration. The longitudinal axis of the bridge after the registration corresponds with the *x*-axis of the global coordinate system.

et al. [55]; ii) for the fracture energy in compression it was adopted a ductility index of 1.60 mm [56]; iii) the tensile strength was taken equal to 5.00% of the compressive strength and; iv) the fracture energy in the tensile regime was assumed as 0.05 N/mm.

The infill layers were modeled obeying to a Mohr-Coulomb failure criterion. For the infill added during the Mediaeval period, it was considered the values proposed by Conde et al. [8], i.e., a friction angle of 30° together with a cohesion of 20 kPa. On the other hand, the *Opus Caementecium* was modeled according to the values proposed by Frunzio et al. [46], i.e., a friction angle of 32° and a cohesion value of 500 kPa.

For the concrete slab added during the last restoration project (see Section 2.1) it was considered a compressive strength of 16.00 N/mm^2 and a tensile strength of 1.90 N/mm^2 according to the Eurocode 2 [57].

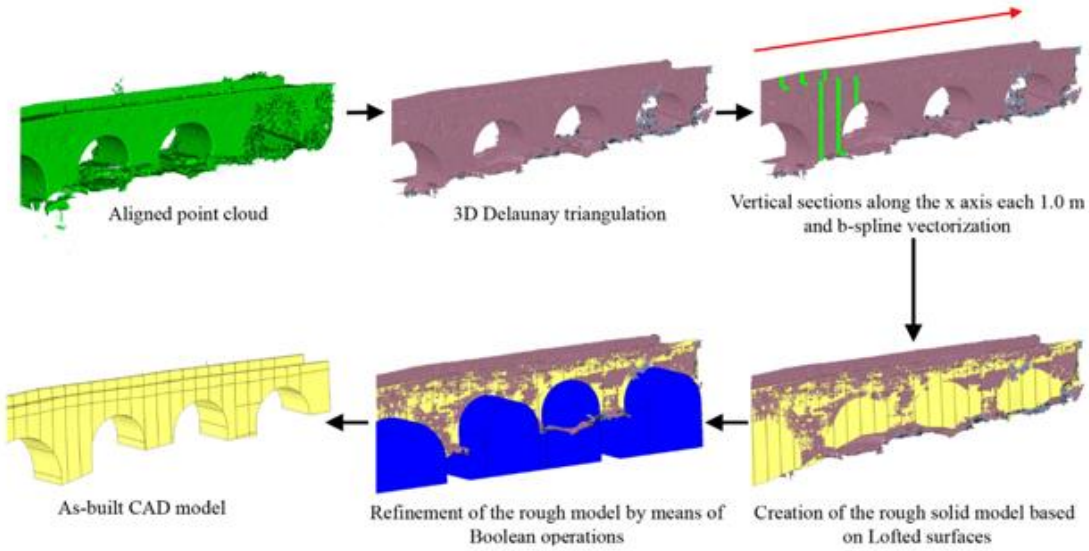

Fig. 18. Proposed workflow for the generation of the as-built CAD model.

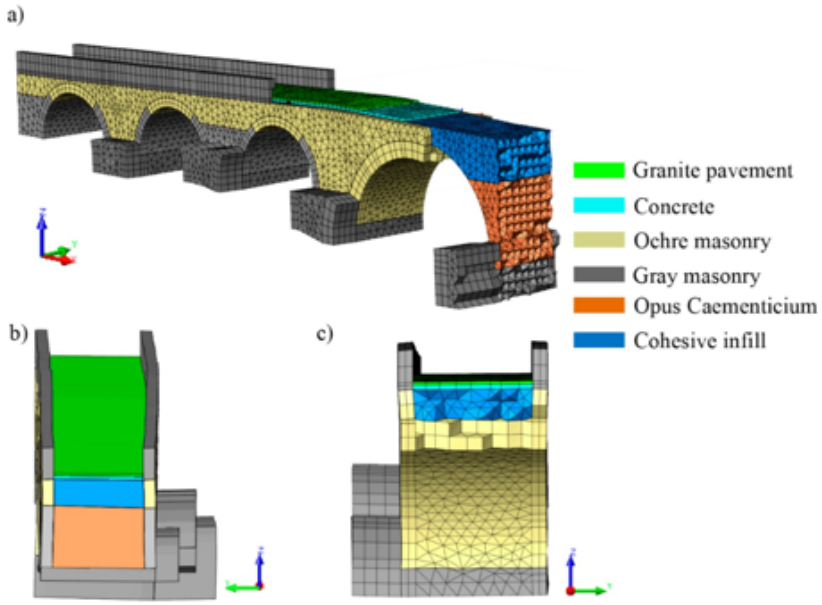

Fig. 19. Finite element mesh: a) general view; b) and c) details of the mesh where it is possible to observe the real captured geometry of the spandrel walls.

Due to the complexity of the model, and the almost null contribution to the overall structural response of the bridge, the granite cobblestone was not explicitly modeled. However, in an attempt to still partially consider it, the mass of this element was added as an external load over the concrete slab. This load had a value of 2.30 kN/m^2.

To obtain the solution of the non-linear problem, the regular (full) Newton-Raphson method, complemented with the line-search technique and the arc-length method in a spherical path, was used. As for the convergence criterion, an energy norm was adopted with a threshold value of 0.001.

6.2. *Safety analysis against vertical loading*

To evaluate the mechanical performance of the bridge, both a non-linear analysis under its self-weight and under an increasing gravitational loading were performed. Both aspects will allow evaluating the current safety condition of the structure against vertical loads. It is noted that the bridge is currently closed to the traffic and in an area with a low seismic hazard. Thus, no analysis under live loads or seismic loading was taken into account within the framework of the present study.

Two different models were used in the numerical simulation procedure, which are categorized as follows: a) Model I: for the analysis of the bridge behavior under its self-weight and; b) Model II: for the evaluation of the performance of the structure under vertical loads. During the numerical simulations, the control node used to track the response of the structure was placed at the mid-line and mid-span of the barrel vault with the higher rise to span ratio (vault number 4).

Thus, concerning the structural behavior of the bridge against its self-weight (Model I), it was observed that the minimum principal (compressive) stresses appeared on an area close to pier number 4, at the springings of the major barrel vault (Fig. 21). The maximum value was around 0.68 MPa, which is pretty far away, 19.00%, of the maximum compressive capacity estimated for the grey granite masonry (around 3.60 MPa). As expected, at this load status the bridge is fundamentally under compression everywhere. Areas with tensile stresses are rather localized, particularly at the upper part of spandrel walls as well as at the mid-span of all barrel vaults. The maximum value for these stresses was approximately 0.10 MPa.

For the case of the Model II, the gravity load was monotonically increased until causing the collapse of the bridge. As a result, the bridge was able to withstand up to seven times its own weight (Fig. 22). This safety factor seems to be related with the high-quality of the different constructive elements (masonry and infill), the weather-tightening concrete placed on the deck (Table 11) and the dimensions of the structure (Table 1). The failure mechanism of the structure is related to the area in between the barrel vaults 3, 4 and 5. In particular, a lateral failure that involves the out-of-plane bending of the spandrel wall between the vaults 3 and 4 is evidenced as a consequence of the high lateral pressures generated by the infill materials. Moreover, significant cracking in the connection between the spandrel wall and the vaults 3–4 can also be observed, as well as longitudinal cracking at the crown of the major barrel vault (number 4) (Fig. 23a). Regarding the compressive stresses status, it is possible to observe some crushing of the masonry in the lower part of the pier that supports the barrel vaults 4 and 5 as well as at the springing of the barrel vault 3 (Fig. 23b).

Table 7
Mechanical properties of the masonries.

Material	Variable	Upper bound	Average value	Lower bound
Grey granite masonry	Young modulus (GPa)	3.60	3.25	2.90
	Poisson ratio (−)	–	0.24	–
	Density (kg/m3)	2500	2250	2000
Ochre granite masonry	Young modulus (GPa)	2.41	2.23	2.05
	Poisson ratio (−)	–	0.26	–
	Density (kg/m3)	2000	1850	1700

Table 8
Mechanical properties of the infill material layers.

Layer	Variable	Upper bound	Average value	Lower bound
1 (cohesive material)	Young modulus (GPa)	0.52	0.48	0.45
	Poisson ratio (−)	–	0.20 [8]	–
	Density (kg/m3)	1771	1768	1764
2 (opus caementicium)	Young modulus (GPa)	1.28	1.03	0.84
	Poisson ratio (−)	–	0.05 [46]	–
	Density (kg/m3)	1852	1837	1821

Table 9
Mechanical properties of the materials of the bridge's deck.

Material	Variable	Upper bound	Average value	Lower bound
Concrete slab	Young modulus (GPa)	–	25.70	–
	Poisson ratio (−)	–	0.20	–
	Density (kg/m3)	–	2400	–
Granite cobblestone	Young modulus (GPa)	–	16.78	–
	Poisson ratio (−)	–	0.20	–
	Density (kg/m3)	–	2318	–

According to these results (and despite the intrinsic uncertainties associated with the accurate determination of the inelastic parameter values), the bridge mechanical performance under vertical loads can be considered fairly satisfactory.

Yet, taking into consideration the focus of the present work: the propose of a multidisciplinary approach able to characterize masonry bridges at the geometrical, material and structural level, a comparative study was also carried out. The aim is confronting the results obtained from the proposed methodology with those that would have been obtained in case of solely considering the values provided by the literature. Accordingly, the values suggested by the Italian code NTC08 [58] were considered. This code provides ranges for the material properties values of different masonry typologies. Herein, both masonries were encapsulated within the class ashlar stone masonry, assuming a Young Modulus of 2.40 GPa for the ochre masonry and 3.20 GPa for the grey masonry. For the infill, it was considered the average values proposed by Conde et al. [8] and Frunzio et al. [46] for the cohesive infill and the *Opus Caementicium*, respectively. Since these values come from the literature a structural knowledge level of LC1 was assumed, with a consequent confidence factor equal to 1.35 [58].

Thereby, with the mechanical properties values provided by the literature, the safety factor of the bridge against vertical loading decreases from 7.3 to 5.5 (25% of reduction) (Fig. 22). Moreover, it is worth mentioning that the failure mechanism shows some discrepancies with respect to the previous model. In this case, the damages associated with the tensile failure of masonry concentrated mainly in vault 4. Indeed, a more intensive cracking at the crown of this element can be appreciated (Fig. 24a). Finally, regarding the compressive stresses status, a similar picture in terms of stress distribution was received (Fig. 24b).

Additionally, several numerical simulations were also carried out with the aim of evaluating the influence of the main structural components, namely masonry and infill, in the global response of the structure. To this end, the mechanical properties of each component were reduced by half (Fig. 22). According to these results, it is possible to observe that both properties have a similar impact in the safety factor; reducing one of them by a half decrease the safety factor of the bridge in about 34%. In spite of this similarity in terms of the safety factor, it was possible to observe that a reduction in the masonry properties leads to a more ductile response in the collapse mechanism development due to the increase of masonry crushing areas (Fig. 22).

6.3. Evaluation of the structural response in case of continuing the material looses

One of the main advantages that can offer an accurate numerical simulation, supported on an extensive experimental campaign, is the

Table 10
Results obtained from the initial numerical simulation.

Mode	Experimental frequency	Numerical frequency	MAC
1	10.30	9.62	0.97
2	14.57	14.39	0.85
3	21.09	20.00	0.97
4	24.13	–	–
5	26.31	24.39	0.94
6	29.45	28.34	0.83
7	31.90	29.95	0.55

Table 11
Updated values obtained after the manual calibration. UB and LB denotes the upper and lower bounds respectively.

	Variable	UB	LB	Update value
Grey granite masonry	Young modulus (GPa)	3.60	2.90	3.60
Ochre granite masonry	Young modulus (GPa)	2.41	2.05	2.41
Cohesive infill	Young modulus (GPa)	0.52	0.45	0.50
Opus Caementicium	Young modulus (GPa)	1.28	0.84	1.28
Interaction soil-bridge	Tangential stiffness in the longitudinal direction (N/m3)	1×10^9	1×10^7	1×10^9
	Tangential stiffness in the transversal direction (N/m3)	1×10^9	1×10^7	1×10^9

Table 12
Results obtained from the updated numerical model.

Mode	Experimental frequency	Numerical frequency	MAC
1	10.30	10.02	0.98
2	14.57	14.95	0.87
3	21.09	20.76	0.96
4	24.13	–	–
5	26.31	25.11	0.95
6	29.45	29.81	0.86
7	31.90	32.11	0.86

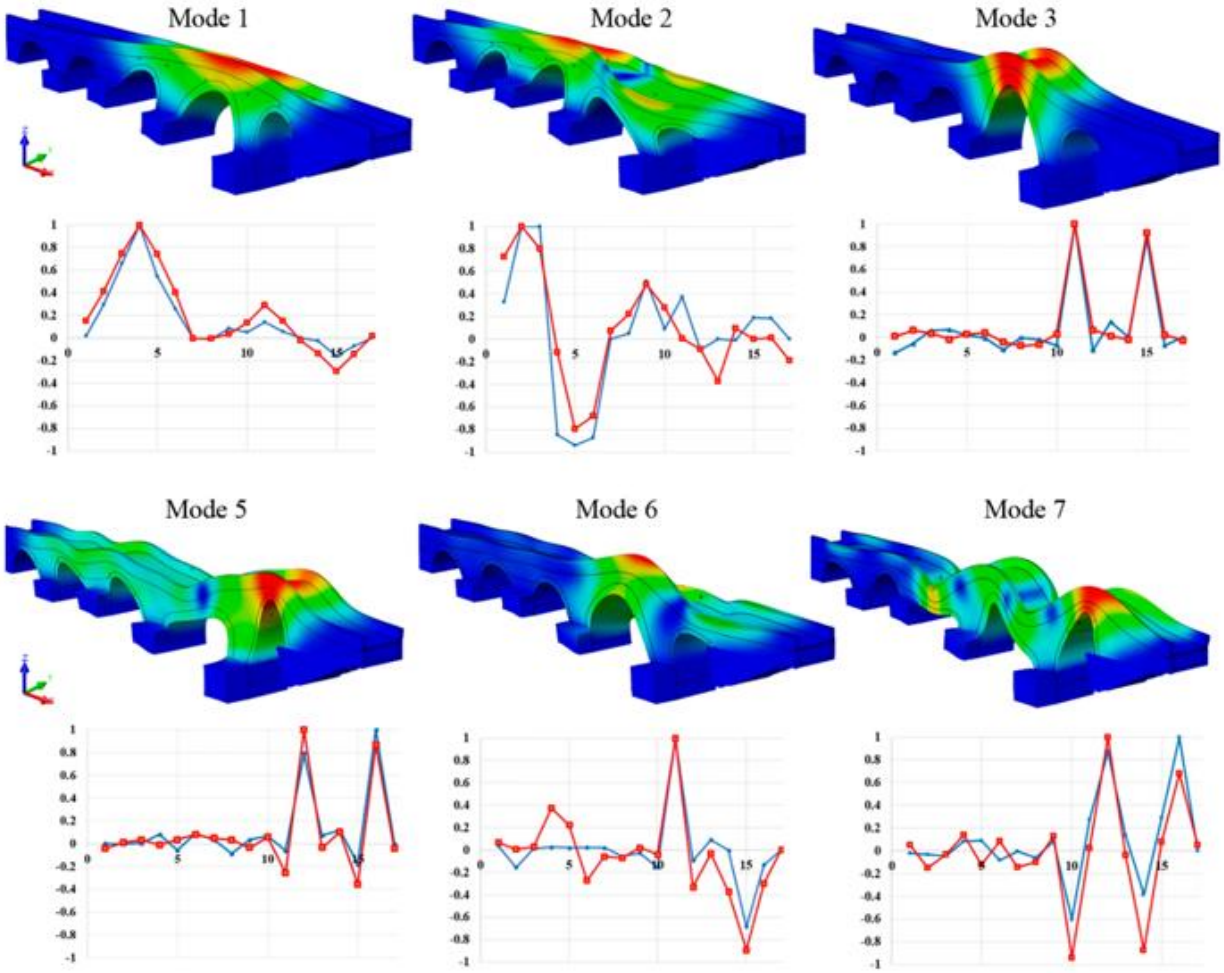

Fig. 20. Results obtained after the manual calibration. The red lines in the graphs represents the numerical normalized modal displacements. The blue lines represent the experimental normalized modal displacements. (For interpretation of the references to colour in this figure legend, the reader is referred to the web version of this article.)

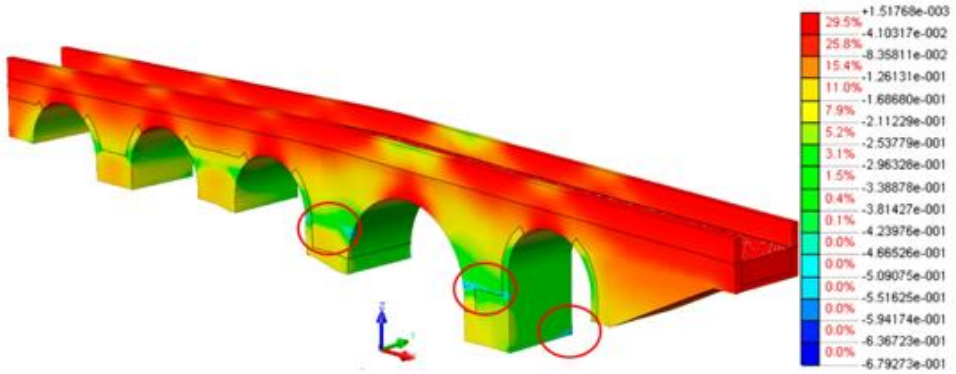

Fig. 21. Contour plot of minimum principal stresses obtained for the Model I (MPa).

possibility of simulating the response of the structure against different hazards such as earthquakes, material losses or pier scours. Therefore, the structure used to validate the proposed multidisciplinary approach was also analyzed against its more probable hazard: the material loses. To this end, the resistance section of both the spandrel walls and vaults were reduced by 25% and 50% (Table 13).

As expected, if the resistance section is reduced, the load-bearing capacity of the bridge is also reduced. On the one hand, if the section is

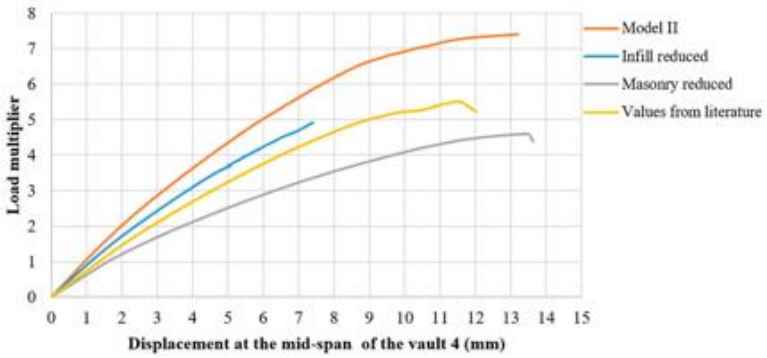

Fig. 22. Load-displacement curves obtained. In orange the response of the bridge in its current configuration. In blue the response of the bridge in case of considering the mechanical properties provided by the literature. In grey and blue the response of the structure in case of reducing by half the masonry and infill properties respectively. (For interpretation of the references to colour in this figure legend, the reader is referred to the web version of this article.)

reduced by 25% the safety factor of the bridge decreases by 13% (from 7.2 to 6.3) (Fig. 25). On the other hand, if the section is reduced by 50% the safety factor decreases by 30% (from 7.2 to 5.2). Thus, based on these results, one might argue that in a medium to a large term the bridge seems to be safe against material losses, mainly due to the high quality of the constituent materials.

As for the collapse mechanism, minor discrepancies were observed with respect to the baseline model (Model II). Thus, for the model that considers a 25% of section reduction, the failure mode is again related to the collapse of the spandrel wall between the barrel vaults 3 and 4, and the tensile cracking of the barrel vault 4 (Fig. 26a). Edge failure of both barrel vaults is again suggested, which is evidenced by the severe concentration of cracks in the form of a staircase pattern going from the springings of the vaults up to ¾ of their rises.

For the model with 50% of section reduction, the collapse mode is mainly related to the consequential and expected weakening of the major barrel vault (vault 4). This way, a severe diagonal crack related to the tensile failure of masonry can be found at the crown (Fig. 26b). Apart from this, a significant bulging of the spandrel wall can also be observed due to the combination of both the high lateral soil pressures generated and the reduction in the section of this element.

7. Conclusions

In this work, a fully non-destructive multidisciplinary approach applied to the structural diagnosis of masonry arch bridges is proposed. This methodology allows a characterization of masonry bridges at different levels: i) geometrical level; ii) material level and; iii) structural

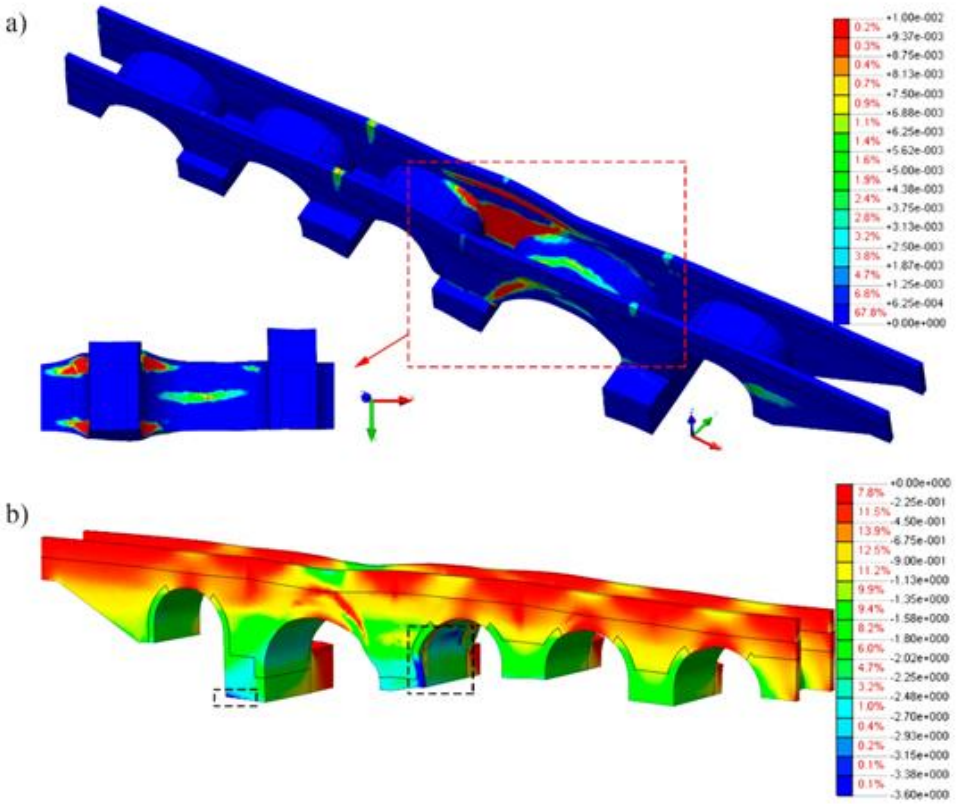

Fig. 23. Deformed shape at failure due to the incremented gravitational loading: a) contour plot of maximum principal strains (indicator of cracking) and; b) contour plot of minimum principal stresses.

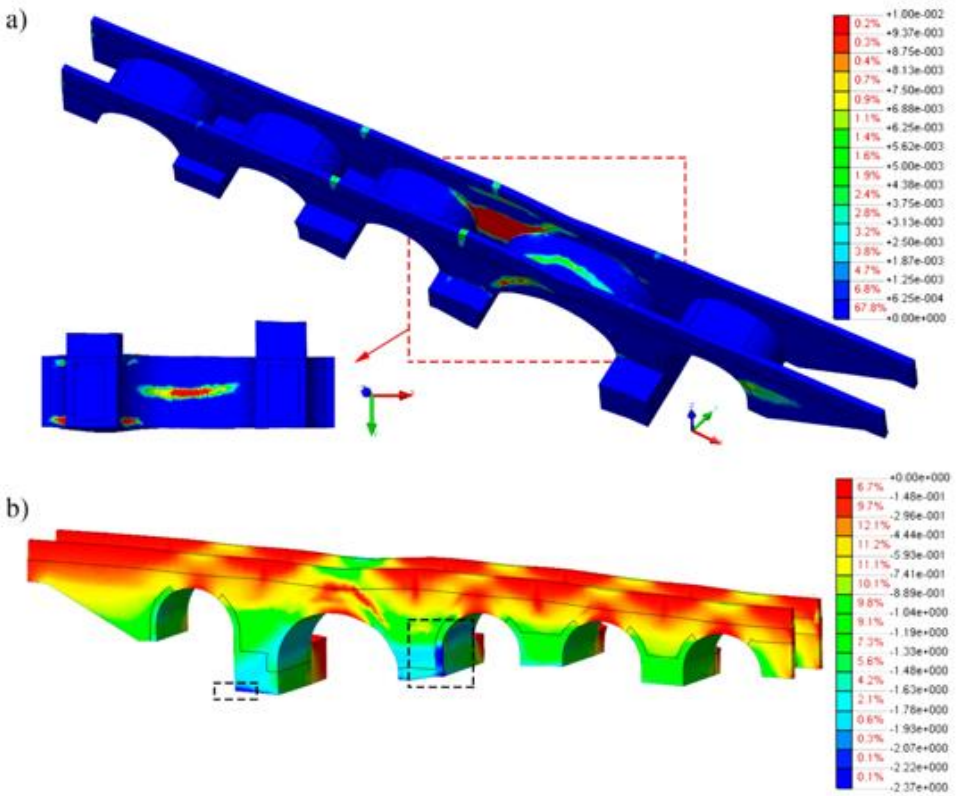

Fig. 24. Results from the numerical model made up by the values provided by the literature [8,46,58]: a) contour plot of maximum principal strains (indicator of cracking) and; b) contour plot of minimum principal stresses.

Table 13
Thicknesses of the spandrell walls and barrel vaults considered.

Element	Original (m)	Reduction of 25%	Reduction of 50%
Vault 1 (West)	0.55	0.41	0.28
Vault 2	0.54	0.41	0.27
Vault 3	0.53	0.40	0.27
Vault 4	0.85	0.64	0.43
Vault 5 (East)	0.55	0.41	0.28
Spandrel wall	0.45	0.34	0.23

level.

From the geometrical point of view, the method uses several well-known approaches such as the terrestrial laser scanner and the ground penetrating radar. These approaches are complemented by several surface waves technologies such as the impact-echo method and the multichannel analysis of surface waves. The former allows evaluating the thickness of the different construction elements (e.g. spandrel walls or vaults). Meanwhile, the latter allows characterizing the inner disposition of the bridge's infill, even in situations in which the ground penetrating radar cannot penetrate. Then, all this data is combined in an as-built CAD model created through the latest means of reverse engineering, i.e. extrusions, boolean operations and Loft surfaces. The combination of these methods allows generating models able to reproduce complex deformations presented in historical constructions.

At the material level, the proposed methodology introduces two surface-waves methodologies. On one hand, the sonic testing for the characterization of the elastic properties of the masonry is proposed. On

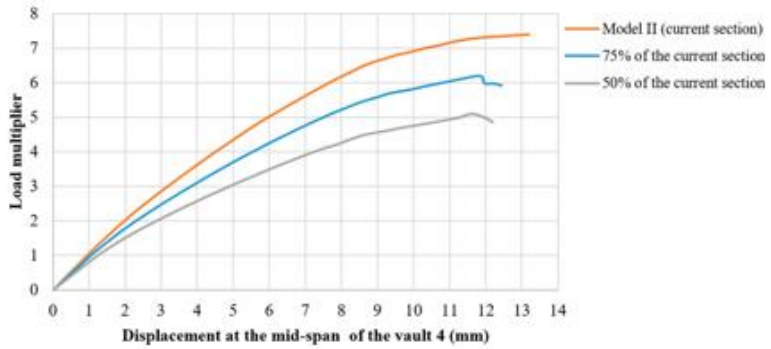

Fig. 25. Load displacement curves obtained during the numerical simulations taking into account possible material loses.

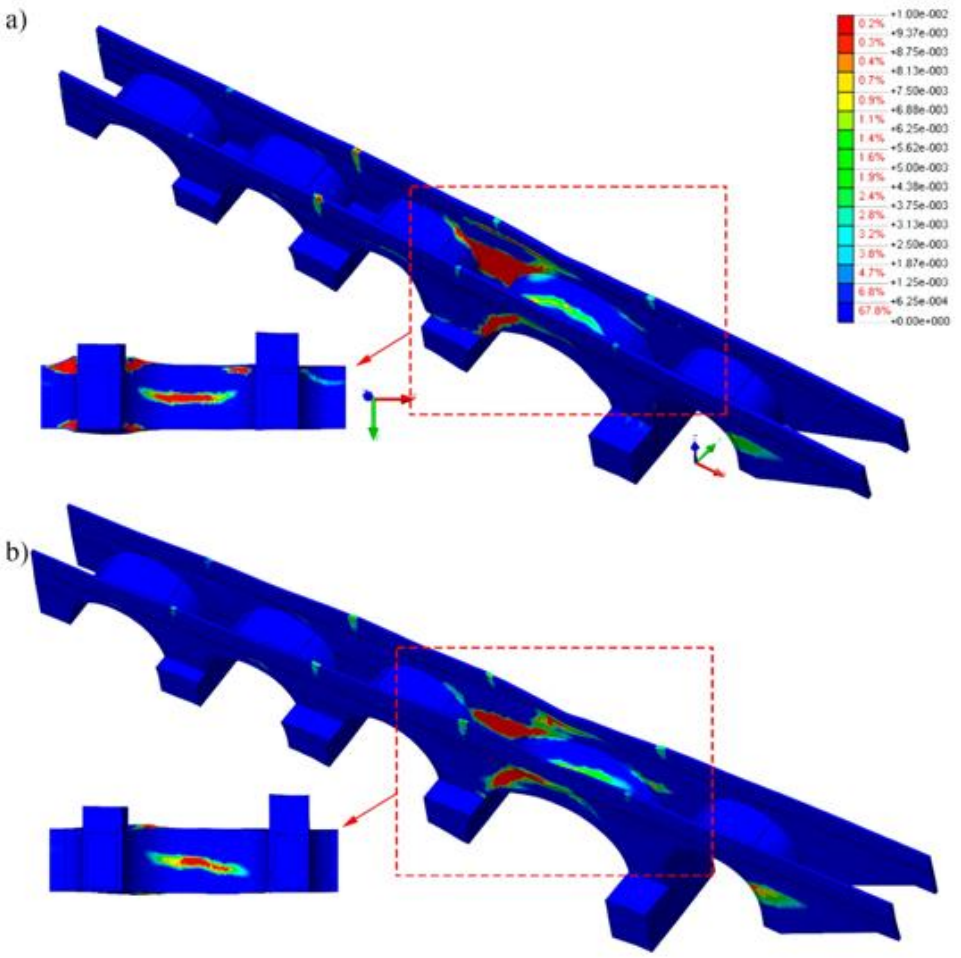

Fig. 26. Results obtained considering a section reduction of the arches and spandrel walls: a) 75% of the original one and; b) 50% of the original one.

the other hand, the multichannel analysis of surface waves is used for the characterization of the Young Modulus and the density of the infill. This method, based on a linear array of geophones, allows creating a 2D profile of the bridge's infill made up by shear-velocities. Both methodologies enable the material characterization of the bridge foregoing the use of invasive techniques.

Finally, the ambient vibration testing was also adopted as a non-destructive technique able to characterize the global response of masonry arch bridges. This technique is used to detect potential mismatches between the real structure behavior and the simulated one.

The combination of all the previously shown methodologies allows generating accurate advanced numerical simulations of masonry arch bridges. In order to evaluate the potentialities and limitations of the proposed methodology, a complex case study was chosen; the Roman bridge over the Adaja River, in Castile and León, Spain. The computational model developed as a result of the proposed methodology was able to capture six of the seven modes detected during the ambient vibration tests. These modes showed an average relative error in frequencies of about 2.22% and an average MAC value of 0.91, corroborating the robustness of the proposed method. Finally, the performance of the structure against vertical loads is evaluated and contrasted with a numerical model created by means of the data obtained in the literature (no experimental data). This comparison highlights the relevance of this methodology, obtaining a discrepancy of 25% in terms of safety factor. Complementary to this evaluation, and taking into consideration the advantages of the finite element method, several numerical simulations were carried out with the aim of evaluating the performance of the bridge in case of ensuing material loses. In all the simulations the results suggest that the bridge has an excellent bearing capacity, being safe in the medium-long term to the material loses that it is suffering.

Futures improvement of the methdodology will be focused on several aspects: i) the use of automatic updating strategies such as those proposed by [8,16,25,27,32] based on genetic and deterministic approaches; ii) further validation of the multichannel analysis of surface waves tests as a potential approach for the analysis of the infill materials and iii) the study of the possible relation between the data provided by the multichannel analysis of surface waves tests and the nonlinear properties of the infill materials.

Acknowledgments

This work was financed by ERDF funds through the V SUDOE INTERREG program within the framework of the HeritageCARE project, Ref. SOE1/P5/P0258 and the research project Patrimonio 5.0 funded by Junta of Castilla y León, Ref. SA075P17. First author would like to thank the University of Salamanca for the program for human resources "Programa II: Contratos Postdoctorales". Authors also wish to thanks to the council of Avila for their support in gathering the historical documentation of the bridge.

References

[1] I. Olofsson, L. Elfgren, B. Bell, B. Paulsson, E. Niederleithinger, J. Sandager Jensen, G. Feltrin, B. Täljsten, C. Cremona, R. Kiviluoma, Assessment of European railway bridges for future traffic demands and longer lives–EC project "sustainable bridges", Struct. Infrastruct. Eng. 1 (2) (2005) 93–100, https://doi.org/10.1080/15732470412331289396.

[2] B. Conde, P. Eguía, G.E. Stavroulakis, E. Granada, Parameter identification for damaged condition investigation on masonry arch bridges using a Bayesian approach, Eng. Struct. 172 (2018) 275–284, https://doi.org/10.1016/j.engstruct.2018.06.040.

[3] C. Modena, G. Tecchio, C. Pellegrino, F. da Porto, M. Donà, P. Zampieri, M.A. Zanini, Reinforced concrete and masonry arch bridges in seismic areas: typical deficiencies and retrofitting strategies, Struct. Infrastruct. Eng. 11 (4) (2015) 415–442, https://doi.org/10.1080/15732479.2014.951859.

[4] V. Sarhosis, S. De Santis, G. de Felice, A review of experimental investigations and assessment methods for masonry arch bridges, Struct. Infrastruct. Eng. 12 (11) (2016) 1439–1464 https://www.tandfonline.com/doi/full/10.1080/15732479.2015.1136655.

[5] P. Zampieri, M.A. Zanini, F. Faleschini, L. Hofer, C. Pellegrino, Failure analysis of masonry arch bridges subject to local pier scour, Eng. Fail. Anal. 79 (2017) 371–384, https://doi.org/10.1016/j.engfailanal.2017.05.028.

[6] A. Arêde, C. Costa, A.T. Gomes, J.E. Menezes, R. Silva, M. Morais, R. Gonçalves, Experimental characterization of the mechanical behaviour of components and materials of stone masonry railway bridges, Constr. Build. Mater. 153 (2017) 663–681, https://doi.org/10.1016/j.conbuildmat.2017.07.069.

[7] A.C. Aydin, S.G. Özkaya, The finite element analysis of collapse loads of single-spanned historic masonry arch bridges (Ordu, Sarpdere Bridge), Eng. Fail. Anal. 84 (2018) 131–138, https://doi.org/10.1016/j.engfailanal.2017.11.002.

[8] B. Conde, L.F. Ramos, D.V. Oliveira, B. Riveiro, M. Solla, Structural assessment of masonry arch bridges by combination of non-destructive testing techniques and three-dimensional numerical modelling: application to Vilanova bridge, Eng. Struct. 148 (2017) 621–638, https://doi.org/10.1016/j.engstruct.2017.07.011.

[9] G. Milani, P.B. Lourenço, 3D non-linear behavior of masonry arch bridges, Comput. Struct. 110 (2012) 133–150, https://doi.org/10.1016/j.compstruc.2012.07.008.

[10] E. Bertolesi, G. Milani, F.D. Lopane, M. Acito, Augustus bridge in Narni (Italy): seismic vulnerability assessment of the still standing part, possible causes of collapse, and importance of the Roman concrete infill in the seismic-resistant behavior, International Journal of Architectural Heritage 11 (5) (2017) 717–746, https://doi.org/10.1080/15583058.2017.1300712.

[11] S. Degli Abbati, A.M. D'Altri, D. Ottonelli, G. Castellazzi, S. Cattari, S. de Miranda, S. Lagomarsino, Seismic assessment of interacting structural units in complex historic masonry constructions by nonlinear static analyses, Comput. Struct. 213 (2019) 51–71, https://doi.org/10.1016/j.compstruc.2018.12.001.

[12] Á. Bautista-De Castro, L.J. Sánchez-Aparicio, L.F. Ramos, J. Sena-Cruz, D. González-Aguilera, Integrating geomatic approaches, operational modal analysis, advanced numerical and updating methods to evaluate the current safety conditions of the historical Bôco Bridge, Constr. Build. Mater. 158 (2018) 961–984, https://doi.org/10.1016/j.conbuildmat.2017.10.084.

[13] J.P.C. Pérez, J.J. de Sanjosé Blasco, A.D. Atkinson, L.M. del Río Pérez, Assessment of the structural integrity of the Roman bridge of Alcántara (Spain) using TLS and GPR, Remote Sens. 10 (3) (2018) 387, https://doi.org/10.3390/rs10030387.

[14] V.N. Moreira, J.C. Matos, D.V. Oliveira, Probabilistic-based assessment of a masonry arch bridge considering inferential procedures, Eng. Struct. 134 (2017) 61–73, https://doi.org/10.1016/j.engstruct.2016.11.067.

[15] M.E. Stavroulaki, B. Riveiro, G.A. Drosopoulos, M. Solla, P. Koutsianitis, G.E. Stavroulakis, Modelling and strength evaluation of masonry bridges using terrestrial photogrammetry and finite elements, Adv. Eng. Softw. 101 (2016) 136–148, https://doi.org/10.1016/j.advengsoft.2015.12.007.

[16] C. Pepi, M. Gioffrè, G. Comanducci, N. Cavalagli, A. Bonaca, F. Ubertini, Dynamic characterization of a severely damaged historic masonry bridge, Procedia engineering 199 (2017) 3398–3403, https://doi.org/10.1016/j.proeng.2017.09.579.

[17] B. Riveiro, J. Caamaño, P. Arias, E. Sanz, Photogrammetric 3D modelling and mechanical analysis of masonry arches: an approach based on a discontinuous model of voussoirs, Autom. Constr. 20 (4) (2011) 380–388, https://doi.org/10.1016/j.autcon.2010.11.008.

[18] B. Riveiro, B. Conde-Carnero, P. Arias-Sánchez, Laser scanning for the evaluation of historic structures, in: M. Khosrow-Pour (Ed.), Laser Scanning for the Evaluation of Historic Structures, Civil and Environmental Engineering: Concepts, Methodologies, Tools, and Applications, IGI Global, Hershey, 2016, pp. 807–835. ISBN-13: 978-1466696198.

[19] B. Conde, L. Díaz-Vilariño, S. Lagüela, P. Arias, Structural analysis of Monforte de Lemos masonry arch bridge considering the influence of the geometry of the arches and fill material on the collapse load estimation, Constr. Build. Mater. 120 (2016) 630–642, https://doi.org/10.1016/j.conbuildmat.2016.05.107.

[20] I. Lubowiecka, P. Arias, B. Riveiro, M. Solla, Multidisciplinary approach to the assessment of historic structures based on the case of a masonry bridge in Galicia (Spain), Comput. Struct. 89 (17) (2011) 1615–1627, https://doi.org/10.1016/j.compstruc.2011.04.016.

[21] B. Riveiro, P. Morer, P. Arias, I. de Arteaga, Terrestrial laser scanning and limit analysis of masonry arch bridges, Constr. Build. Mater. 25 (4) (2011) 1726–1735, https://doi.org/10.1016/j.conbuildmat.2010.11.094.

[22] M. Korumaz, M. Betti, A. Conti, G. Tucci, G. Bartoli, V. Bonora, A.G. Korumaz, L. Fiorini, An integrated Terrestrial Laser Scanner (TLS), Deviation Analysis (DA) and Finite Element (FE) approach for health assessment of historical structures. A minaret case study, Eng. Struct. 153 (2017) 224–238, https://doi.org/10.1016/j.engstruct.2017.10.026.

[23] A.M. D'Altri, G. Milani, S. de Miranda, G. Castellazzi, V. Sarhosis, Stability analysis of leaning historic masonry structures, Autom. Constr. 92 (2018) 199–213, https://doi.org/10.1016/j.autcon.2018.04.003.

[24] S.G. Barsanti, G. Guidi, A geometric processing workflow for transforming reality-based 3D models in volumetric meshes suitable for FEA, The International Archives of Photogrammetry, Remote Sensing and Spatial Information Sciences 42 (2017) 331–338, https://doi.org/10.5194/isprs-archives-XLII-2-W3-331-2017.

[25] L.J. Sánchez-Aparicio, B. Riveiro, D. Gonzalez-Aguilera, L.F. Ramos, The combination of geomatic approaches and operational modal analysis to improve calibration of finite element models: a case of study in Saint Torcato Church (Guimarães, Portugal), Constr. Build. Mater. 70 (2014) 118–129, https://doi.org/10.1016/j.conbuildmat.2014.07.106.

[26] G. Castellazzi, A.M. Altri, G. Bitelli, I. Selvaggi, A. Lambertini, From laser scanning to finite element analysis of complex buildings by using a semi-automatic procedure, Sensors 15 (8) (2015) 18360–18380, https://doi.org/10.3390/s150818360.

[27] E. Bassoli, L. Vincenzi, A.M. D'Altri, S. de Miranda, M. Forghieri, G. Castellazzi, Ambient vibration-based finite element model updating of an earthquake-damaged masonry tower, Struct. Control. Health Monit. 25 (5) (2018) e2150, , https://doi.org/10.1002/stc.2150.

[28] R. Aguilar, M.F. Noel, L.F. Ramos, Integration of reverse engineering and non-linear numerical analysis for the seismic assessment of historical adobe buildings, Autom. Constr. 98 (2019) 1–15, https://doi.org/10.1016/j.autcon.2018.11.010.

[29] M. Solla, R. Asorey-Cacheda, X. Núñez-Nieto, B. Conde-Carnero, Evaluation of historical bridges through recreation of GPR models with the FDTD algorithm, NDT & E International 77 (2016) 19–27, https://doi.org/10.1016/j.ndteint.2015.09.003.

[30] A. Arce, L.F. Ramos, F.M. Fernandes, L.J. Sánchez-Aparicio, P.B. Lourenço, Integrated structural safety analysis of San Francisco master gate in the fortress of Almeida, International Journal of Architectural Heritage 12 (2017) 761–778, https://doi.org/10.1080/15583058.2017.1370507.

[31] C. Costa, A. Arêde, M. Morais, A. Aníbal, Detailed Fe and DE modelling of stone masonry arch bridges for the assessment of load-carrying capacity, Procedia Engineering 114 (2015) 854–861, https://doi.org/10.1016/j.proeng.2015.08.039.

[32] C. Costa, D. Ribeiro, P. Jorge, R. Silva, A. Arêde, R. Calçada, Calibration of the numerical model of a stone masonry railway bridge based on experimentally identified modal parameters, Eng. Struct. 123 (2016) 354–371, https://doi.org/10.1016/j.engstruct.2016.05.044.

[33] The Charter of Krakow: principles for conservation and restoration of built heritage, Available on-line at http://smartheritage.com/wp-content/uploads/2015/03/KRAKOV-CHARTER-2000.pdf , Accessed date: April 2019.

[34] I. Lubowiecka, J. Armesto, P. Arias, H. Lorenzo, Historic bridge modelling using laser scanning, ground penetrating radar and finite element methods in the context of structural dynamics, Eng. Struct. 31 (11) (2009) 2667–2676, https://doi.org/10.1016/j.engstruct.2009.06.018.

[35] A. Blanco Freijeiro, Informes académicos. Puente romano sobre el río Adaja, en Ávila, Boletín de la Real Academia de la Historia 182 (1) (1985) 144–145. Available on-line at: http://www.cervantesvirtual.com/obra/informes-acadmicos-puente-romano-sobre-el-ro-adaja-en-vila-0/ , Accessed date: April 2019.

[36] M.C. Tomás, La manipulación del patrimonio cultural: la Fábrica de Harinas de Ávila, Polit. Soc. 27 (1998) 89–116. Available on-line at: http://revistas.ucm.es/index.php/POSO/article/view/POSO9898130089A , Accessed date: April 2019.

[37] HeritageCARE-Report 1.1: Survey of Construction Systems, Type of Damages and Deterioration Processes within the SUDOE Territory, Available on-line at http://heritagecare.eu/wp-content/uploads/2017/09/HeritageCARE-Report-1.1.pdf , Accessed date: April 2019.

[38] J. García-Talegon, A.C. Iñigo, S. Vicente-Tavera, E. Molina-Ballesteros, Heritage stone 5. Silicified granites (bleeding stone and ochre granite) as global heritage stone resources from Ávila, Central Spain, Geosci. Can. 43 (1) (2016) 53–62, https://doi.org/10.12789/geocanj.2016.43.087.

[39] L.J. Sánchez-Aparicio, S. Del Pozo, L.F. Ramos, A. Arce, F.M. Fernandes, Heritage site preservation with combined radiometric and geometric analysis of TLS data, Autom. Constr. 85 (2018) 24–39, https://doi.org/10.1016/j.autcon.2017.09.023.

[40] M. Franaszek, G.S. Cheok, C. Witzgall, Fast automatic registration of range images from 3D imaging systems using sphere targets, Autom. Constr. 18 (3) (2009) 265–274, https://doi.org/10.1016/j.autcon.2008.08.003.

[41] N.J. Carino, The impact-echo method: An overview, ASCE World Structural Engineering Conference, 2001, pp. 1–18. Available on-line at: https://www.nist.gov/publications/impact-echo-method-overview , Accessed date: April 2019.

[42] L. Miranda, L. Cantini, J. Guedes, A. Costa, Assessment of mechanical properties of full-scale masonry panels through sonic methods. Comparison with mechanical destructive tests, Struct. Control. Health Monit. 23 (3) (2016) 503–516, https://doi.org/10.1002/stc.1783.

[43] G. Grandjean, I. Cousin, M. Seger, J. Thiesson, S. Lambot, B. Van Wesemael, A. Stevens, K. Samyn, A. Bitri, S. Bernardi, From Geophysical Parameters to Soil Characteristics, Available on-line at https://pdfs.semanticscholar.org/832b/3bef86f6889d7bd8dfa268f5bd7d23365bce.pdf?_ga=2.47695463.1384578154.1554894584-921443786.1548157246 , Accessed date: April 2019.

[44] C.B. Park, R.D. Miller, J. Xia, Multichannel analysis of surface waves, Geophysics 64 (3) (1999) 800–808, https://doi.org/10.1190/1.1444590.

[45] L. Knopoff, Observation and inversion of surface-wave dispersion, Tectonophysics 13 (1–4) (1972) 497–519, https://doi.org/10.1016/0040-1951(72)90035-2.

[46] G. Frunzio, M. Monaco, A. Gesualdo, 3D FEM analysis of a roman arch bridge, Historical Constructions, 2001, pp. 591–598. Available on-line at: http://www.csarmento.uminho.pt/docs/ncr/historical_constructions/page%20591-598%20_

69_.pdf , Accessed date: April 2019.
[47] L. Pelà, A. Aprile, A. Benedetti, Comparison of seismic assessment procedures for masonry arch bridges, Constr. Build. Mater. 38 (2013) 381–394, https://doi.org/10.1016/j.conbuildmat.2012.08.046.
[48] R. Brincker, L. Zhang, P. Andersen, Modal identification from ambient responses using frequency domain decomposition, The International Society for Optical Engineering (2000) 625–630. Available on-line at: https://vbn.aau.dk/ws/files/12765845/Modal_Identification_from_Ambient_Responses_using_Frequency_Domain_Decomposition , Accessed date: April 2019.
[49] J. Wang, D. Gu, Z. Yu, C. Tan, L. Zhou, A framework for 3D model reconstruction in reverse engineering, Comput. Ind. Eng. 63 (4) (2012) 1189–1200, https://doi.org/10.1016/j.cie.2012.07.009.
[50] D.I.A.N.A. TNO, DIANA User's Manual, Release 10.2, Available on-line at: https://dianafea.com/manuals/d102/Diana.html, (2017) , Accessed date: April 2019.
[51] EN 1996-1-1, Eurocode 6: Design of Masonry Structures—Part 1-1: General Rules for Reinforced and Unreinforced Masonry Structures, Comité Européen de Normalisation (CEN), Available on-line at https://www.phd.eng.br/wp-content/uploads/2015/02/en.1996.1.1.2005.pdf, (2005) , Accessed date: April 2019.
[52] J. García Talegón, A.C. Iñigo, M. Vicente Hernández, M. Vargas, J.L. Pérez Rodríguez, E. Molina Ballesteros, Granites employed in Ávila-Spain. I. Chemical composition of the different types, Mater. Constr. 44 (233) (1994), https://doi.org/10.3989/mc.1994.v44.i233.594.
[53] EN 1992-1-1, Eurocode 2: Design of Concrete Structures - Part 1–1: General Ruels and Rules for Buildings, Comité Européen de Normalisation (CEN), 2005 Available on-line at: https://www.phd.eng.br/wp-content/uploads/2015/12/en.1992.1.1.2004.pdf , Accessed date: April 2019.
[54] R.J. Allemang, The modal assurance criterion (MAC): twenty years of use and abuse, Sound and vibration 37 (8) (2003) 14–23. Available on-line at: http://www.sandv.com/downloads/0308alle.pdf , Accessed date: April 2019.
[55] M. Tomaževič, Earthquake-Resistant Design of Masonry Buildings, first ed., Imperial College Press, London, 1999 (978-1-84816-083-5).
[56] P. Lourenço, Recent advances in masonry structures: Micromodelling and homogeneization, in: U. Galvanetto, M.H. Ferri Aliabadi (Eds.), Multiscale Modeling in Solid Mechanics: Computational Approaches, Imperial College Press, London, 2009, pp. 251–294. ISBN-13: 978-1848163072.
[57] G. Toniolo, M. di Prisco, Reinforced concrete design to Eurocode 2, first ed., Springer, London, 978-3-319-52033-9, 2017.
[58] Ministerio delle infrastructure e dei trasporti, Norme tecniche per le costruzioni, Decreto Ministeriale del 14, 2008 Available on-line at: http://www.cslp.it/cslp/index.php?option=com_content&task=view&id=66&Itemid=1 , Accessed date: April 2019.